This paper can be found at: https://doi.org/10.1016/j.engstruct.2022.115116

# An effective numerical modelling strategy for FRCM strengthened curved masonry structures

*Anna Castellano[1], Aguinaldo Fraddosio[2], Daniel V. Oliveira[3], Mario D. Piccioni[2], Eleonora Ricci[2,*], Elio Sacco[4]*

## Abstract

Fabric Reinforced Cementitious Matrix (FRCM) composites are currently considered a very effective solution for strengthening masonry constructions. However, the mechanical interactions governing the response and the strength of FRCM reinforced masonry structures are very complex, especially in the case of curved structures. Moreover, these interactions involve several interfaces between different materials. Thus, the development of accurate numerical models for curved FRCM reinforced masonry structures comes up against several difficulties, and models too complex for practical applications can be obtained. In addition, several mechanical parameters needed for the calculations are generally inaccessible by conventional experimental tests.

Here, a suitable numerical modelling strategy for FRCM strengthened curved masonry structures is proposed to combine the accuracy in simulating the actual behaviour in terms of stiffness, strength and collapse mechanisms with a reasonable simplicity, making the proposed approach usable also by practitioners, by adopting commercial codes and at a moderate computational effort. The relatively small number of mechanical parameters characterizing the model can be determined by ordinary experimental tests on materials or by literature formulations.

The proposed modelling strategy is validated with respect to experimental data found in literature concerning a FRCM reinforced masonry barrel vault, and then is employed for studying the seismic capacity of the vault through a pushover analysis. A broad sensitivity analysis sheds light on the effect of variations of the mechanical parameters on the predicted overall behaviour, showing the robustness of the results obtainable through the proposed approach concerning inaccuracies in the determination of the parameters often very difficult to determine by ordinary experimental tests on masonry structures.

## Keywords

Masonry, vault, FRCM, numerical modelling.

[1]Department of Mechanics, Mathematics and Management, Polytechnic University of Bari, Via Orabona, 4, 70125, Bari, Italy. E-mail: anna.castellano@poliba.it

[2]Department of Civil Engineering Sciences and Architecture, Polytechnic University of Bari, Via Orabona, 4, 70125, Bari, Italy. E-mail: aguinaldo.fraddosio@poliba.it, mariodaniele.piccioni@poliba.it, eleonora.ricci@poliba.it

[3]Department of Civil Engineering, University of Minho, ISISE, Campus de Azurém, 4800-058 Guimarães, Portugal. E-mail: danvco@civil.uminho.pt

[4]Department of Structures for Engineering and Architecture, University of Naples Federico II, Via Claudio 21, 80125, Naples, Italy. E-mail: elio.sacco@unina.it

*Corresponding author.

# 1. Introduction

Fiber reinforced composites have been widely used in the last decades for strengthening masonry structures because of their high strength-to-weight ratio, low invasiveness and relatively easy installation procedure. Recently, composites made of an inorganic matrix generally reinforced with short fibers and embedding continuous fibers (glass, carbon, PBO fibers and steel cords) in form of fabric gained relevance as strengthening materials, especially for historic constructions [1,2], in addition to other conventional techniques [3]. These composites are known as Fabric Reinforced Cementitious Matrix (FRCM) or Textile Reinforced Matrix (TRM) composites; in what follows, the denomination "FRCM" will be adopted.

The mechanical behaviour and the failure modes of FRCMs significantly differ from that of the most established Fiber Reinforced Polymers (FRP) composites due to a different kind of matrix. First, the stress-strain response of FRCM composites under uniaxial tension is mainly trilinear, with each branch corresponding to a different damage level (undamaged, cracking of the matrix and final damage of the fiber net) [4–6], whilst the FRP behaviour is mainly linear up to failure. Second, the fabric-matrix bond strongly depends on the inorganic matrix penetration between the filaments of the fabric, hindered by the presence of binder grains with a large diameter. Ineffective penetration might lead to the so-called "telescopic failure" of the composite in tension, not observed for FRP composites [7,8]. Finally, it has been experimentally observed that the friction among grains provides the matrix-substrate interface of residual strength, also not observed for FRP composites [9,10]. For the above, models developed for FRP composites cannot be used to properly describe the mechanical behaviour of FRCM composites.

Experimental and numerical study on the application of FRCM composites for strengthening masonry structures, especially for arches and vaults, is still the object of ongoing research. In particular, different numerical procedures for representing FRCMs mechanical behaviour have been proposed in the literature to date, based either on macro- or micro-modelling approaches. A feature generally common to both approaches is the modelling of the FRCM-substrate interaction using non-linear interface elements.

In some recent research works on FRCM reinforced masonry, a macro-modelling approach is adopted both for the masonry substrate and the composite. For example, in [11] a glass FRCM system is modelled with shell elements using the Total Strain Crack model and assuming experimental curves (multilinear in tension and parabolic in compression). In [12] a similar approach is used, and plane stress elements were employed for the composite, bonded to a panel by inelastic interface elements to represent the possible debonding of the FRCM.

A micro-modelling description has been proposed in [13] and [14]; the fiber net and the mortar layers constituting the matrix are modelled separately. The mechanical behaviour of the matrix is described by a smeared cracking approach, namely the Concrete Damage Plasticity model in [13] and the Total Strain Crack model in [14]. A relevant difference is that in [13] fibers and matrix are separately modelled, whereas in [14] a special shell element formulated for reinforced concrete and embedding bar elements is used. Moreover, in [13] an elastic-perfect plastic behaviour is assumed for the fibers while in [14] the behaviour of the bars is considered linear elastic up to the failure. Notice that both in [13] and [14] no interfaces are considered between the composite and the masonry substrate.

The complexity of the non-linear phenomena to be described, often strictly interconnected, yields the risk of developing models too complex for practical applications, useable only by the research community. Indeed, for the needs of practitioners, numerical models should depend on a reasonable number of mechanical parameters to be evaluated by conventional experimental tests and/or deduced by acknowledged values or empirical laws in literature. Furthermore, it is very important to know in advance how inaccuracies in the determination of these parameters can affect the final results in terms of the overall response of the structure. In this vein, the purpose of this research is to develop a modelling strategy for FRCM reinforced curved masonry structures able to combine the suitability of use by practitioners with a sufficiently accurate description of the mechanical behaviour in terms of stiffness, peak loads, failure modes and post-peak behavior, generally strongly dependent from the interactions between reinforcement and masonry support in terms of stress transfer and of bond integrity. To this aim, it is relevant not only the ease of the model, but also the use of constitutive laws characterized by a relatively small number of mechanical parameters, consistent with that evaluable by conventional experimental tests, or by new experimental approaches, still under investigation [15,16].

The paper contains a review of the modelling approaches for masonry strengthened with FRCMs and a brief discussion on the mechanical behaviour of masonry arches and barrel vaults reinforced with FRCM composites (Section 2), being the main features of the developed modelling strategy described in Section 3. Then, a representative case study is considered from the literature and used as the reference for validating the modelling approach and for discussing its effectiveness (Section 4-5). The results obtained by the numerical simulation are presented and discussed in Section 6, including a comparison with the experimental results. A broad sensitivity analysis is performed in Section 7 to study the overall response of the reinforced structure. Indeed, a numerical model for a complex structural system like a FRCM-reinforced masonry requires inevitably several mechanical parameters. In principle, in practical applications, it is needed to experimentally determine all of these parameters with the greatest possible accuracy. Anyway, for some parameters, this can be challenging if not unfeasible. On the other hand, not all the material parameters have the same influence on the predicted structural response: therefore, the sensitivity analysis is useful for understanding which of the mechanical parameters needs to be carefully determined to have representative numerical results; while a rough estimate starting from literature values or formulations can be adopted for the remaining without significantly affecting the accuracy of the results. Finally, in Section 8 the proposed modelling strategy has been applied to the evaluation of the seismic capacity of the examined reinforced masonry vault through a pushover analysis.

## 2. Modelling FRCM-reinforced curved masonry structures: an overview

Experimental campaigns on FRCM retrofitted masonry arches and vaults [17–23] show that due to the presence of the reinforcement, high compressive stresses may develop in curved masonry structures, leading to the crushing of masonry, very uncommon for unreinforced structures and, at high load levels, sliding of masonry blocks along mortar joints might occur since FRCM reinforcements also allow for the development of substantially higher shear stresses.

The bond at the composite-substrate interface plays a crucial role in the collapse mechanism. Debonding is here understood as a partial damage process that weakens the bond between different materials (like, e.g., the masonry substrate and the reinforcement layer), while detachment means the complete loss of bond, involving the separation between the materials. The failure of arches and barrel vaults strengthened at the extrados or intrados can be due to the debonding at the matrix-substrate interface, associated with the cracking of the matrix where the reinforcement prevents the formation of hinges typical of the collapse mechanism of unstrengthened arches. As the load increases, transversal cracks appear and propagate from the external matrix layer to the inner layer up to the masonry substrate; then, tangential stresses, $\tau_{nt}$, develop at the matrix-substrate interface. In addition, stresses normal to the reinforced masonry surface, $\sigma_n$, develop to radially equilibrate the shear stresses $\tau_{nt}$ (see Fig. 1). In particular, for reinforcements at the intrados, these normal stresses negatively affect the composite-support bond capacity, thus facilitating the debonding, which can lead to the composite detachment. This phenomenon doesn't occur for reinforcements applied at the extrados, where the effect of the curvature is beneficial to the overall strength.

In particular, [24] reports experimental and analytical studies about the influence of the masonry substrate curvature on the bond capacity of carbon FRCM and Steel Reinforced Grout (SRG). The study is conducted on suitable specimens having curvatures simulating intrados reinforcements. It is shown that, as the curvature increases, both the bond strength and the ultimate displacement decrease because of the normal stresses developing at the matrix-substrate interface (the reduction is more marked for SRG).

In general, the failure of arches strengthened at the extrados is due to the sliding along joints and the detachment of the reinforcement at one of the abutments [18,19,25]. The failure is also associated with the cracking of the matrix and the debonding at the matrix-substrate interface where the reinforcement prevents the formation of hinges. The breaking of the reinforcement fiber grid has been reported for a structure where steel anchor plates were used [26] to fix the strengthening system at the masonry support. On the other hand, the failure of arches and barrel vaults strengthened at the intrados is generally characterized by the debonding of the reinforcement near the load application point [27]. The use of spike anchors or steel anchors prevents the reinforcement detachment but might result in the fracture of the matrix and the rupture of the fibers [19] .

Although arches and vaults represent fundamental structural elements in masonry construction, the development of simple and effective numerical models of these elements reinforced with FRCM composites appears limited in the literature. Among them, [28] proposes a numerical model for FRCM reinforced masonry arches, represented by a set of rigid plates interacting through unidirectional links and connected to the substrate employing interface elements. In [29], a SRG strengthening layer for a masonry arch was modelled by equivalent two-node truss elements perfectly bonded at the extrados of the arch. Although the above numerical models succeed in describing the contribution of the reinforcement in terms of increased load carrying capacity and ductility and in reproducing the debonding of the reinforcement, they were not able to model the cracking of the matrix observed near the collapse. In [30] the mechanical behaviour of an arch externally strengthened with PBO-FRCM composites, experimentally studied in [25], was numerically simulated by modelling the composite as a system of two layers of mortar matrix held together by an inelastic interface and connected to the arch through another interface. This way, both the matrix-fibers delamination and debonding at the composite-substrate can be described. Moreover, for the matrix, a smeared cracking model was employed to consider the occurrence of cracks. Schemes of the aforementioned numerical approaches for FRCM reinforced masonry arches and vaults are reported in Fig. 2. Moreover, in [31] the influence of the values of mechanical parameters on the limit horizontal load for masonry arch bridges reinforced at the intrados by FRCM composites is discussed. Finally, in [32] also the influence of settlements is studied.

For a model to be sufficiently representative of the mechanical behaviour, it should consider the following key aspects: debonding of the composite at the composite-substrate interface; cracking of the matrix; sliding of the fiber at the matrix-fiber interface; sliding and crushing of the blocks; influence of the substrate curvature on the overall behaviour. Also, the presence of anchors increasing the bond between FRCM reinforcements and masonry, or of the infill are aspects to be conveniently represented in simulations.

# 3. Proposed modelling strategy

Based on the analysis of the literature, here an effective modelling strategy is proposed for curved masonry structures strengthened with FRCM composites, aimed at representing the relevant mechanical aspects at a relatively low computational cost. This strategy is formulated in a way suitable for being adopted in commercial codes, and thus to make the model available for practical applications. To this aim, modelling choices have been oriented towards the limitation of the number of the required mechanical parameters. The proposed modelling strategy has the advantage to be suitable for the implementation in some commercial codes, like DIANA FEA, here considered, and therefore can bring immediate advantages for improving the accuracy of calculations in practical applications concerning FRCM-reinforced masonry structures. Moreover, it allows determining the main mechanisms inducing the failure of a reinforced arch and the material models to adopt for simulating its response.

## *3.1. Modelling approach*

The idea is to adopt a simplified micro-modelling approach for the substrate to describe also the sliding of the blocks, and of considering the composite as a continuum (representing the matrix) reinforced with bars representing the textile, and having the same cross-section and elastic modulus of the textile. No relative displacements are considered between the textile and the matrix. The bond of the FRCM strip to the curved structure (from now on termed as "vault") is reproduced by interface elements.

Although the FRCM components (matrix and textile) are modelled separately, the assumption of coupling between the matrix and the embedded bar prevents one of the most complex ingredients of micro-modelling approaches, the representation of the matrix-fiber interfaces. Therefore, the adopted approach for the composite cannot be strictly defined as a micro-model. Indeed, even though the slippage of the fibers inside the matrix cannot be directly reproduced, the effects of debonding phenomena occurring at the matrix-fiber interface on the overall structural behaviour can be still indirectly taken into account. As an example, consider the FRCM composite beam element shown in Fig. 3 subjected to axial tensile load. In the configuration adopted for determining the tensile capacity of the FRCM, evaluated as described in [23], a test set-up with clamping-grip configuration is employed [33,34]. Assuming the presence of initial localized damage, as depicted in Fig. 3a, the fracture propagates towards the reinforcement bar and localizes around it when the beam is axially elongated. Cracks appear in the matrix generally where the reinforcement hinders the opening of hinges. The cracks progressively propagate towards the reinforcing fiber net and localize around it. Therefore, debonding phenomena at the matrix-fiber net interface can take place. Indeed, this kind of mechanism happens in FRCM composites applied on vaults.

From the numerical point of view, if the FRCM composite is modelled as a continuum embedding a bar, using a smeared cracking model for the matrix, it can be shown that assuming a perfect bond between the bar and the matrix, or introducing matrix-fiber grid interfaces, should provide comparable results in terms of stresses, displacements and failure mode. To this aim, a sample of

This paper can be found at: https://doi.org/10.1016/j.engstruct.2022.115116

FRCM composite 60 mm × 30 mm × 10 mm made of a lime mortar with a glass fiber mesh embedded is considered. To reproduce the presence of localized fracture, the cross-section labelled $S_2$ (Fig. 3d) is characterized by a reduced area (150 mm$^2$) with respect to any other typical cross-section located at the distance $z$ from the reference cross-section, like $S_1$ in Fig. 3c, having the area 300 mm$^2$. The fractures are positioned symmetrically with respect to the $z$ axis and are 2.5 mm in length (along the $y$ axis). They run through the whole cross-section parallel to the $x$ axis, as reported in Fig. 3d. The $S_2$ cross-section was located at the center of the sample; anyway, numerical experiments performed show that moving the position of $S_2$ provided that there is sufficient distance from the basis does not influence the results.

A 2D plane stress model is adopted to investigate the propagation process of the damage in the cementitious matrix and the effect of the fiber mesh presence inside the composite under axial tension. The sample is supposed to be fixed at one end and a prescribed displacement is imposed at the opposite end to force the composite to stretch up to 0.02 mm. Two modelling approaches are used and compared: a macro-modelling approach (Fig. 3a), with the fiber mesh modelled as a bar embedded in a continuum characterized by the mechanical properties of the composite, and a micro-modelling approach (Fig. 3b), with the composite modelled as two layers of matrix bonded through interfaces to the reinforcement bars, which represent the fiber mesh. Indeed, here the goal is not that of validating the modeling strategy concerning the results of an experimental tensile test, but that of comparing the two numerical strategies.

In both the macro-model and the micro-model, the matrix is modelled with the Total Strain Rotating Crack model assuming the mechanical properties listed in Table 6 (see Section 3.2 for more details). The bar is linear elastic with a Young modulus equal to 78900 MPa. In the macro-model no bond-slip relation is considered to model the contact at the matrix-bar interface, while in the micro-model the matrix is connected to the reinforcement bar using two non-linear interfaces modelled using the Discrete Cracking model. The mechanical parameters assumed for the matrix-bar (MB) interfaces are listed in Table 1.

Fig. 4 shows the Cauchy total stresses recorded in the simulations for a point of the matrix (P1) and a point of the reinforcement bar (P2) for both models. It is easily seen that these results are practically superimposed. As the load gradually increases, the stresses in the matrix and the bar also increase and cracks appear in the matrix in the proximity of the ending tip of the fracture on both sides of the sample. When the axial displacement reaches the value of 0.01 mm, the cracks have already developed in the matrix up to the reinforcement bar, where the stresses suddenly increase, while the stresses in the matrix slightly decrease and then remain almost constant, due to the stress transfer from the matrix to the bar. Fig. 5a and 5b show the distribution of cracks at the final step of the calculations, for the prescribed displacement equal to 0.019 mm.

It is worth noting that some cracks in the macro-model run parallel to the bar (see the zoom of Fig. 5a), revealing that, as a consequence of the propagation of the fracture from the external layer of the composite toward the bar, cracks can occur at the bar-matrix contact surface and debonding phenomena can take place. A similar result is obtained for the micro-model (see Fig. 5b), where rotated cracks appear near the reinforcement bar and shear relative displacements increase at the bar-matrix interface. Thus, it is possible to claim that the results provided by the two models are well comparable and that the assumption of a perfect bond between the bar and the matrix does not fail in indirectly reproducing also the debonding phenomena, which may occur in FRCM composites at the fiber mesh-matrix interface, possible especially when the reinforcement is applied at the extrados.

In conclusion, this modelling choice combines the use of mechanical parameters that can be reasonably determined by practitioners in real applications with the capability of taking into account both the loss of bond at the composite-substrate (directly) and the loss of bond at the matrix-textile (indirectly).

### 3.2. *Simplified micro-modelling for the masonry substrate*

In the framework of simplified micro-modelling approaches, the mortar joint is not represented with its actual thickness (see Fig. 6), but it is considered as a zero thickness interface where cracks can potentially occur and open [35]. The benefit of this simplification in terms of computational costs is high since the number of interfaces needed is halved.

For unreinforced masonry structures, bricks are often modelled as linear elastic blocks since the stresses hardly ever overcome the compressive nor the tensile strength, and the collapse of the structure is mainly due to the opening of fractures at the joints. Since the reinforcement can yield substantially higher stresses, here bricks are modelled by using a smeared cracking damage model, suitable to describe distributed crack patterns, when the specific location of fractures cannot be predicted, as for the case of crushing or tensile failure of bricks. In particular, the Total Strain Rotating Crack model [36] is adopted.

Following [37], the response in compression is represented by a parabolic constitutive law, governed by the compressive strength $f_c$ and by the compressive fracture energy $G_{fc}$. The response in traction is assumed linear elastic up to the tensile strength $f_t$; by further increasing the tensile strains, an exponential softening phase follows [38], ruled by the following expression:

$$\frac{\sigma_{nm}^{cr}\left(\varepsilon_{nm}^{cr}\right)}{f_t}=\exp\left(-\frac{\varepsilon_{nm}^{cr}}{\varepsilon_{nm,ult}^{cr}}\right) \tag{1}$$

where $\sigma_{nm}^{cr}\left(\varepsilon_{nm}^{cr}\right)$ is the crack stress, $\varepsilon_{nm}^{cr}$ is the crack strain and $\varepsilon_{nm,ult}^{cr}$ is the ultimate crack strain (see Fig. 7a).

Eight-node square plane stress elements (CQ16M) are used (Fig. 7b) for the masonry units.

The Discrete Cracking model is adopted to describe the brick-brick (BB) interface mechanical behaviour. This interface model is based on the total deformation theory where initiation, Mode-I behaviour and Mode-II behaviour are independently specified (uncoupled modes). [44]An exponential stress-strain law is assumed for modelling the decreasing of the stress as the cracks opening grows when the material is subjected to tractions. This stress-strain law is well suited also for masonry-like materials since an exponential behaviour is reported in [39] for the cracks opening in mortar joints of masonry panels in traction.

The Discrete Cracking model is ruled, in the elastic phase, by the normal stiffness ($k_n$) and tangent stiffness ($k_t$) with respect to the interface plane according to the following relation:

$$\mathbf{t}=\begin{bmatrix} k_n & 0 \\ 0 & k_t \end{bmatrix}\Delta\mathbf{u}, \tag{2}$$

where $\mathbf{t}=\{\sigma, \tau\}^{\mathrm{T}}$ is the traction vector and $\Delta\mathbf{u}$ is the vector collecting the relative interface displacement. The tensile softening of the interface response (see Fig. 8a) is described by an exponential function depending on the interface tensile strength and the tensile fracture energy [40]:

$$\frac{\sigma}{f_t} = f(\delta) - \frac{\delta}{\delta_0} f(\delta_0), \tag{3}$$

where

$$f(\delta) = \left[1 + \left(3\frac{\delta}{\delta_0}\right)^3\right] exp\left(-6.93\frac{\delta}{\delta_0}\right) - \left(28\frac{\delta}{\delta_0}\right) exp(-6.93), \tag{4}$$

$\sigma$ is the stress at the interface, $f_t$ is the interface tensile strength, $\delta$ is the crack opening, obtained by subtracting from the total deformation the sum of the elastic deformation and of a contribution which takes into account non-elastic effects during unloading of the material adjacent to the crack surfaces, and $\delta_0$ is the crack opening for which stress can no longer be transferred. The crack opening $\delta_0$ is determined starting from the interface tensile strength $f_t$ and the mode I fracture energy $G_{ft}^{I}$ .

The shear stress τ is supposed to reduce after cracking. Denoting by $w$ the crack width and $s$ the crack slip, it is assumed that

$$\begin{cases} \tau = k_t s & for\ w \leq \dfrac{\sigma}{k_n} \\ \tau = \beta k_t s & for\ w > \dfrac{\sigma}{k_n}, \end{cases} \tag{5}$$

with β the shear retention factor varying between 0 and 1. In particular, for β=1 the shear response after cracking is still described by (5.1), without any reduction of the shear stresses. On the contrary, for β=0, no shear stresses are transmitted after cracking, as for the case of smooth crack surfaces. When β assumes a value between 0 and 1, a reduced shear modulus is assumed after cracking, and the shear stresses never go to zero describing the effect of the sliding friction between the crack surfaces that ensures stress transferring residual capacity to the interface.

Six-node interface elements, labelled CL12I, are used in the adopted mesh for describing BB interfaces (see Fig. 8b-c).

### *3.2. FRCM modelling*

The strengthening FRCM composite, made of a cementitious mortar reinforced by short fibers and embedding a fiber net, is described as a continuum reinforced by suitable bar elements representing the fiber net. The primary goal is to reproduce the overall effects of the cracking of the matrix and the tensile strength provided by the combination of the matrix and the fiber net. Therefore, the same smeared cracking damage model employed for the brick, the Total Strain Rotating Crack model, is considered here for reproducing the nucleation and evolution of cracks in the continuum (the matrix). The tensile softening behaviour is described by the JSCE model [41], considering a stress plateau after cracking, followed by a softening phase ruled by the equation

$$\sigma = f_t \left(\frac{\varepsilon_{tu}}{\varepsilon}\right)^c, \tag{6}$$

with σ the tensile stress, ε the total tensile strain, $f_t$ the tensile strength, $\varepsilon_{tu}$ the tensile strain corresponding to the end of the plateau, and $c$ an exponent, usually set as 0.4 for unreinforced concrete and as 0.2 for reinforced concrete elements. It has been shown in [14] that the JSCE model is capable to simulate the response of FRCM composites in traction; in fact, the plateau before the softening phase reproduces the tension stiffening effect observed in the matrix of FRCM composites during the crack propagation phase, when cracks develop in the matrix and the load is progressively transferred from the matrix to the fiber mesh. Indeed, eq. (6) represents a residual tensile strength and a smoother reduction of the tensile stresses, typical of FRCM composites, if compared to other softening models like eq. (1), more suitable for unreinforced masonry. For the applications of interest of the present paper, the description of the FRCM matrix behaviour in compression has no practical interest: therefore, a simple linear elastic response can be considered.

To model the mechanical response of the FRCM, a special element implemented into DIANA FEA is adopted. It is an eight-node plane stress element with reinforcement bars embedded inside. Since the displacements and the strains of the bars and the continuum elements are fully coupled, it results in a contribution of the bars in terms of stiffness, tensile strength and ductility of the continuum. Moreover, the bar elements play a leading role in withstanding the tensile stresses transmitted by the vault to the composite when the matrix cracks.

The input data for reinforcement bars comprise the Young modulus ($E_f$), the stress-strain law under uniaxial traction and the geometrical properties, i.e., the cross-section area.

### 3.3. *Brick-FRCM interface modelling*

The interaction between the FRCM composite and the substrate is described by an interface, labelled CS (composite-substrate), using again the Discrete Cracking model described in Section 3.1, also suitable for reproducing the detachment of the composite from the substrate, which might occur due to the debonding at the composite-substrate interface.

## 4. Case study and determination of the mechanical parameters

### 4.1. *Reference case-study*

The proposed numerical approach is applied for simulating the experimental behaviour observed in an *in-situ* test of a masonry barrel vault retrofitted at the extrados with glass FRCM composites. The results of the experimental tests are presented in [23], where the load-carrying capacity of the reinforced vault is compared to that of an unstrengthened vault having the same geometrical and mechanical features. For convenience of the reader, the main experimental results in [23] are briefly summarized.

The examined structure is a barrel vault characterized by the geometrical data reported in Table 2 and subjected to a concentrated load at a distance of 556mm from the left abutment (approximately one fourth of the span).

In Fig. 9a and b, the geometry of the model is reported along with the position of the hinges opened during the in-situ test of the FRCM reinforced vault. Notice that the hinges corresponding to angles $\alpha_1$ and $\alpha_4$ are not located at the impost of the vault, as one would expect. This discrepancy can be explained by Fig. 1(c) of [23]. This figure shows that the cuts made on the existing vault for obtaining the part to be reinforced by FRCM, and then to be tested, do not reach the two timber beams constituting the imposts. Therefore, the actual span of the tested FRCM reinforced vault is reduced with respect to the internal span of 2555 mm between the two timber beams (see also Fig. 2(b) of

[23]). In particular, by considering the actual position of the hinges at the extremity of the vault, an actual span of 1934 mm has to be considered for calculations (see Fig. 9c).

Due to the small thickness of the vaults, the test on the unstrengthened structure (from here on indicated as "UV") was performed under load control by sequentially putting sandbags on the extrados of the vault that weighed 4-7 kg each, up to the collapse. The reinforced vault (from here on indicated as "RV") was tested in displacement control by means of a hydraulic jack connected to a load cell with a maximum capacity of 100 kN. Four loading and unloading cycles were performed on the FRCM retrofitted vault, the first two useful for the settling of the experimental setup and the further two for investigating the beginning of the non-linear phase of the vault response. In Fig. 10 the load-displacement experimental curves for UV and RV are reported.

The above described experimental provision concerning the load application and the execution of load cycles have not been reproduced in numerical simulations because of the complexity in accounting for the contact surface imperfections in the numerical model. Therefore, numerical analyses for both UV and RV are numerically performed under displacement control according to a monotonically increasing displacement history.

The unstrengthened vault (UV) collapsed as a four-hinge mechanism. According to [23], the first hinge ($H_1$) appeared at the extrados, under the load application point. The second hinge ($H_2$) opened at the intrados at a symmetric position with respect to the first hinge; the third and the fourth hinges ($H_3$, $H_4$) occurred at the left and right abutments, respectively (see the scheme in Fig. 10). No information is provided about the load levels corresponding to the opening of the hinges.

The collapse mechanism of the reinforced vault (RV) was characterized by the formation of one hinge ($H_1$) under the load application area for about 1800 N, while the second hinge ($H_2$) occurred at about 3/4 of the vault span, at a load of 2100 N and at a symmetric position concerning $H_1$. The occurrence of $H_2$ was revealed by the cracking of the composite that prevented the complete opening of the hinge. When the third and the fourth hinges formed at the abutments, the vault collapsed due to slippage phenomena at the fiber-matrix interface and the debonding of the reinforcement at the left support (see schemes in Fig. 10). The third and the fourth hinges formed after the peak load.

# 5. Case study and determination of the mechanical parameters

## 5.1. *Reference mechanical parameters*

The mechanical characterization of the masonry and the glass FRCM reinforcement was carried out by means of experimental tests on the bricks, the mortar, the cementitious matrix, the fibers and the whole reinforcement system. The main experimental data are listed in Table 3, where the subscripts have the following meanings: "*b*" stands for "brick", "*mj*" for "mortar joint", "*f*" for "fiber", "*lm*" for "lime mortar"; moreover, "*c*" stands for "compressive", "*t*" for "tensile", "*s* for "shear", "*d*" for "debonding", and are used for the characterization of the mechanical parameters governing the numerical model, as specified below.

It is worth noting that the test reported in [23] was performed on a masonry specimen cut from the unreinforced vault; thus, it is reasonable to assume that the cutting processing of the specimen from the structure may have induced a disturbance in the material.

The composite tensile properties plotted in Figure 10 are the schematization of the results of tensile tests performed by [23] using the clamping-grip configuration reported in [33,34]. In the following Subsections, the results of the experimental tests are employed for characterizing the constitutive laws used in the proposed model strategy. When experimental results are not available, suitable literature values or formulations are considered.

*5.2. BB interface*

According to the Discrete Cracking model, the mechanical parameters required to define the behaviour of the BB interface are the normal stiffness $k_{BBn}$, the tangent stiffness $k_{BBt}$, the tensile strength $f_{mjt}$, the tensile fracture energy $G_{mjft}$ and the reduced shear modulus $G_{BB}$.

The normal and tangent stiffness cannot be determined from the experimental tests usually performed for the mechanical characterization of materials. In [42] a relation is proposed for the definition of the normal stiffness of BB interfaces as a function of the Young's moduli of the bricks and the mortar of the joints, $E_b$ and $E_{mj}$ respectively, and of the thickness $h_{mj}$ of the mortar joint:

$$k_{BBn} = \frac{E_b E_{mj}}{h_{mj}(E_b - E_{mj})} \tag{7}$$

Notice that according to [43] eq. (7) gives accurate results only if the Young's modulus of the brick is sufficiently higher than that of the mortar, otherwise an unrealistically high normal stiffness is obtained. A similar formula is also proposed in [42] for the determination of the tangent stiffness $k_{BBt}$ as a function of the shear modulus of the bricks and mortar, $G_b$ and $G_{mj}$, respectively. When the latter data are not available, $k_{BBt}$ can be assumed equal to about 40% of the normal stiffness $k_{BBn}$, as suggested in the literature [44,45].

In the present case, the reference paper [23] reports (see Table 3) the average Young's modulus of the bricks $E_b$=2016 MPa, the average Young's modulus of the mortar obtained from a test on a masonry specimen cut from the unreinforced vault $E_{mj}$=321.5 MPa, and the average thickness of the joint $h_{mj}$=10 mm. Therefore, eq. (7) yields a normal stiffness of the BB interface $k_{BBn}$=38.25 N/mm$^3$. Assuming the tangent stiffness $k_{BBt}$ of the BB interface to be 40% of $k_{BBn}$, one obtains $k_{BBt}$=15.3 N/mm$^3$.

Notice that the pictures reported in [23] show that the thickness of the joints is very variable along the vault; this could affect somewhat the reliability of the obtained values of $k_{BBn}$ and $k_{BBt}$. Nevertheless, in absence of direct experimental results on the stiffness of the joints, the value determined by eq. (7) is considered.

To verify the reliability of the above reported values of $k_{BBn}$ and $k_{BBt}$, a numerical simulation of the load-displacement behaviour of the unreinforced vault is performed (see the blue continuous curve in Fig. 12, labelled UV). In the same figure, the experimental load-displacement curve is the red continuous line. The upper bound for the collapse load obtained by the kinematic theorem of Limit Analysis with reference to the actual hinges position at the collapse, see Fig. 9, is also reported (dashed black line, corresponding to 254 N). The considered values of $k_{BBn}$ and $k_{BBt}$ give a response comparable with the experimental results[23], and compatible with Limit Analysis results, since the latter are obtained neglecting the tensile strength of joints [46].

The interface tensile strength, $f_t$, which rules the onset of the interface opening, does not correspond to the tensile strength of the mortar and depends on the bond between the bricks and the mortar joint, which is generally lower. In absence of experimental results, in [47] the tensile strength $f_{mjt}$=0.02 MPa for the BB interface has been determined for the same UV under investigation through a large number of numerical calibration experiments. Therefore, the above value was adopted for the interface tensile strength.

Experimental data for the tensile fracture energy $G_{mjft}$ are not available. It is experimentally observable that the tensile fracture energy tends to increase when the tensile strength increases. Therefore, the tensile fracture energy $G_{mjft}$=0.012 Nmm/mm$^2$ suggested in [48] is considered.

Finally, as explained in Section 2.1, assigning a value of the reduced shear modulus corresponds to providing a value of the shear retention factor β, and therefore assuming that the shear stress between the blocks never vanishes. In absence of specific experimental results, it was deemed appropriate not relying on the residual capacity of transmitting shear stresses after cracking, thus adopting a very low value of the reduced shear modulus $G_{BB}$=0.01 MPa. This value is close to zero, but not zero for avoiding numerical problems. In summary, the values of the BB interface mechanical parameters considered for the computations are reported in Table 4.

### *5.3. CS interface*

The CS interface describes the contact interactions between the substrate bricks and the cementitious matrix. The mechanical parameters required for characterizing the Discrete Cracking model for CS interface are the normal stiffness $k_{CSn}$, the tangent stiffness $k_{CSt}$, the tensile strength $f_{it}$, the tensile fracture energy $G_{ift}$ and the reduced shear modulus $G_{CS}$.

For what concerns the normal stiffness $k_{CSn}$, no experimental data are available. Anyway, since the matrix is characterized by a higher Young's modulus with respect to the mortar used for the joints and to the bricks (see Table 3), the CS normal stiffness is expected to be higher than the BB normal stiffness. Applying eq. (7) to the matrix-substrate system and considering the average Young's moduli of the bricks $E_b$=2016 MPa, the Young's modulus of the lime mortar $E_{lm}$=6080 MPa, and a thickness $h_i$=10 mm for the composite layer, a rounded value $k_{CSn}$=300 N/mm$^3$ is obtained. Again, the tangent stiffness is conventionally fixed in the 40% of $k_{CSn}$, resulting $k_{CSt}$=120 N/mm$^3$.

Regarding the tensile strength of the CS interface $f_{it}$, in [23] the bond strength $\sigma_{bd}$ between the reinforcement and the substrate has been experimentally evaluated by means of pull-off tests on 3 masonry specimens extracted from the vault after the collapse of the structure, with reference to two different configurations. In the first configuration, providing $\sigma_{bd}$=0.17 MPa, the reinforcement was applied only on the brick, while in the second configuration the reinforcement was applied both on the brick and the mortar joint. In the latter case, which provides a much more realistic situation, a far lower bond strength $\sigma_{bd}$=0.05 MPa has been obtained (see Table 3), being here assumed for the tensile strength of the CS interface.

The tensile fracture energy $G_{ift}$ of the CS influences the global behaviour of the composite with respect to debonding phenomena and, thus, the post-peak behaviour of the structure. In particular, a low value of $G_{ift}$ compared to the value assumed for $f_{it}$ leads to a brittle behaviour of the interface and, consequently, to a sudden increase in the relative displacements of the interface. Here $G_{ift}$ is evaluated for a value of the ductility index $d_{iu}$=$G_{ift}/f_{it}$=0.145 mm, determined according to the indication for composite-masonry interfaces reported in [49]. This way, the value $G_{ift}$=0.0072 N/mm is obtained.

Finally, for the same arguments reported in Section 5.2 for BB interface, a very low value of the reduced shear modulus $G_{CS}$=0.01 MPa is considered. In summary, the values of the CS interface mechanical parameters reported in Table 5 are considered.

### *5.4.* FRCM *composite*

The FRCM matrix is modelled as a continuum and the embedded fiber net is represented by bar elements with no degree of freedom on their own. Therefore, even if the FRCM components are distinctly represented, the fibers and the matrix behave as a single element having mechanical properties representative of the whole composite. Therefore, the behaviour of the embedded bars corresponds to that experimentally observed for the composite regarding the third phase of the trilinear stress-strain relation in [23] (see also Fig. 11). In particular, the bar is modelled as linear up to failure, having the stress-strain relation shown by the blue dashed curve in Fig. 11, with Young modulus equal to that of the composite in the third phase of the average trilinear stress-strain curve (blue continuous curve in Fig. 11; $E_f$=78900 MPa). The ultimate tensile stress is identified with the average ultimate stress reached by the composite in tension ($\sigma_f$=595 MPa). Notice that in Table 4 of [23] both data on the Young modulus and the tensile strength are referred to the cross-section of the fiber grid.

In Table 6 the mechanical properties considered for the Total Strain Rotating Crack model describing the behaviour of the FRCM composite are listed. In particular, the Young's modulus $E_c$ was experimentally determined in [23]. For the Poisson's ratio $\nu_c$, a typical value for the employed FRCM is assumed, while the mass density of the composite $\rho_c$ is determined starting from the mass density of the fibers and the matrix and taking into account the mass percentage of each component in the composite.

The tensile strength of the composite $f_{ct}$ does not coincide with that of the mortar constituting the cementitious matrix since it accounts for the mutual collaboration between the matrix and the fiber net. Anyway, these two values are quite similar. Notice that also the Young's modulus of the FRCM composite $E_c$=6500 MPa is slightly different from that of the matrix $E_{\mathrm{matrix}}$=6080 MPa. In Table 4 of [23] are reported data related to the tensile behaviour of the FRCM system under consideration, represented in Fig. 11. In particular, the stress over the whole section of the reinforcement (matrix and fiber net) at the end of the so-called phase I is indicated. Starting from this value, the tensile strength of the composite $f_{ct}$=2.08 MPa has been determined in [23].

The JSCE tension stiffening model requires the definition of the tensile strain corresponding to the end of the plateau, $\varepsilon_{cu}$, and the power parameter $c$. For the latter, experimental results for FRCM composites are well represented choosing $c$ in the range 0.4÷0.8. In particular, the former value is suggested in [14] for a fitting experimental response; therefore, $c$=0.4 is assumed. Since the experimental behaviour shown in Fig. 11 indicates the absence of an appreciable stress plateau, the value $\varepsilon_{cu}$=0.00032 representing the deformation at the end of the elastic range is considered.

No data are available regarding the compressive strength of the FRCM; therefore, the compressive strength of the lime mortar used for the matrix $f_{cc}$=7.48 MPa is considered. Similarly, no experimental values are available for the compressive fracture energy $G_{cc}$. Thus, $G_{cc}$ is estimated by following the Model Code 90 indications for concrete [50]. In particular, if $f_{cc}$ < 12 MPa, $G_{cc}$ can be determined assuming a ductility factor $d_{cc}=G_{cc}/f_{cc}$=1.6 mm, thus obtaining $G_{cc}$=11.97 N/mm. In conclusion, the mechanical parameters considered for characterizing the Total Strain Rotating Crack model adopted for the FRCM composite are summarized in Table 6.

### *5.5. Masonry bricks*

The mechanical tests on the masonry carried out in [23] provide most of the parameters required for the numerical model (see Table 3). In particular for the bricks, the Young's modulus $E_b$=2016 MPa and the compressive strength $f_{bc}$=10.7 MPa, along with the tensile strength obtained by Brazilian tests $f_{bt}$=0.8 MPa, are considered. The Poisson's ratio is set $\nu_m$=0.2, a typical value for clay bricks [51]. The mass density of the clay bricks is considered 1800 kg/m$^3$.

For the determination of the compressive fracture energy, the Model Code 90 recommendations can be used; in particular, for $f_{bc}$<12 N/mm$^2$ a compressive fracture energy $G_{bc}$=17.12 N/mm is obtained. For what concerns the tensile fracture energy $G_{bft}$, as reported in [52] in case of clay bricks and the absence of specific information, the average value 0.029 mm can be assumed for the ductility index $d_{bu}=G_{bft}/f_{bt}$. Therefore, the value $G_{bft}$=0.0232 N/mm is assumed. All the mechanical parameters considered for the masonry bricks are listed in

Table 7.

# 6. Main case study results

Fig. 13 shows the main results in terms of the load-displacement curves; the experimental results are plotted with a dashed line and the numerical results obtained by the proposed model strategy are represented with a continuous line (blue lines for UV and red lines for RV). The numerical simulations of the strengthened vault (RV) yields results consistent to the experimental ones both in terms of collapse load and displacement at the collapse, intended as the displacements at the peak load, see also Table 8. Moreover, the proposed modelling strategy gives representative results also for the case of the unreinforced vault (UV), although the displacement at the collapse is quite different.

As recalled in Section 3, the numerical model is composed of 928 8-node plane stress elements of 15x10 mm$^2$ and 276 6-node interface elements of 15x15 mm$^2$ (termed as mesh 1). Further refinements of the mesh yield a very limited variation of the numerical results despite higher computational costs. As a representative example of the sensitivity analyses performed, Fig. 13 shows also the results obtained by considering 8-node 7.5 mm x 3.3 mm plane stress elements for the matrix and 8-node 7.5 mm x 7.5 mm plane stress elements for the bricks for a total number of 4096 8-node plane stress elements and 552 6-node interface elements (termed as mesh 2). It is seen that the curves corresponding to “mesh 1” and “mesh 2” are practically superimposed up to the peak load and modestly differ in the post-peak phase. However, “mesh 2” required more than twice the time for the analysis.

It is worth recalling that the approach followed here is that of identifying the values of the mechanical parameters by a “blind” processing of the available data; only values directly estimated by experimental tests on the materials or determined according to literature formulations were considered for the calculations. No calibrations of the parameters in view of reproducing the (known) experimental response of the structure have been made.

## *6.1. Reinforced vault (RV)*

The numerical behaviour of the reinforced vault is practically linear up to a load of about 1300 N, slightly lower than the value at which the formation of the first hinge has been experimentally detected. Then, as the load increases, a slight loss of stiffness occurs because of the gradual opening of the first hinge located under the loading application point ($H_1$ in Fig. 14), and of the appearance of the first crack at the abutments. After the peak (2204 N), the load suddenly decreases to 2060 N, corresponding to a 3.4 mm displacement of the load application point. At the same time, a sudden increase in the tangential relative displacement for the CS interface at the left abutment is observed. Then, the load gradually decreases as a progressive debonding of the reinforcement from the left abutment occurs ($H_3$ in Fig. 14), and more cracks appear in the matrix in the centre-right of the vault, where the reinforcement hinders the opening of the hinge $H_2$ (see Fig. 14). This behaviour is comparable to that observed in the experiments. Also, the softening branch of the load-displacement curve obtained from the numerical analyses follows with a good approximation of the experimental curve.

In the sequence, the reinforcement in correspondence of $H_2$ completely cracked and the debonding at the left abutment extended to all the abutment length, causing the detachment of the FRCM strip from the left abutment. In this phase, a displacement of about 7.5 mm is obtained, and the load tends to remain almost constant as the displacement increases.

At the end, the reinforcement starts to detach also from the right abutment (hinge $H_4$ in Fig. 14) because of the debonding at the CS interface. In this last phase, the numerical curve is slightly more sustained than the experimental one, but differences are not relevant.

Table 8 reports the numerically and experimentally collapse load (peak load) for the reinforced vault along with the corresponding displacement of the load application point. It is seen that the numerically estimated collapse load is practically coincident with the experimental one (the difference is of about 0.2%).

For what concerns the displacement of the load application point at the collapse, it is worth recalling that the experimental testing considered four loading-unloading cycles, two in the elastic range and two out of the elastic range. In particular, the last cycle has been performed until the appearance of the first hinge, and produced a residual displacement of 0.65 mm. These loading-unloading cycles are not numerically reproduced for the reasons explained in Section 5.

In Table 8, the difference between the experimental and numerical displacement of the load application point at the collapse for the RV is 0.66 mm. This difference corresponds almost exactly with the above reported residual displacement experimentally observed in the last loading-unloading cycle. Therefore, it is reasonable to think that the difference is only because numerical simulations do not reproduce the cyclic part.

A good agreement between the numerical and the experimental response curves of the RV in Fig. 13 can be noted, also considering that the loading and unloading cycles performed in the experimental tests have not been reproduced in numerical simulations. The lower initial stiffness of the simulated response with respect to the experimental response can be explained since, as recalled in Section 5.1, the elastic parameters of the masonry measured in the experiments and then assumed in the numerical model correspond to that of a damaged material, because of the way the samples were extracted.

For the CS and the BB interfaces described by the Discrete Cracking model, the distribution of relative displacements in the direction normal to the interface cracks are represented in Fig. 14a. The figure clearly shows that the highest displacement values are concentrated in correspondence of the first hinge $H_1$ and at the left abutment, where the debonding of the composite takes place ($H_3$). The distribution of the (smeared) cracks in the materials described by the Total Strain Rotating Crack model, i.e., the bricks and the matrix, can be represented by the normal stresses in the local direction across the crack, see Fig. 14b. This figure reveals that the deformation of the vault before the collapse caused the cracking of the composite at a position symmetric with respect to $H_1$; moreover, FRCM cracks also at the right support and in the proximity of the area near $H_3$ and $H_4$. This was also observed during the *in-situ* tests in the position $H_2$ in Fig. 10. Some cracks formed also in the masonry blocks at the abutments.

In Fig. 15a the load is related to the number of the (smeared) cracks in the bricks and the reinforcement matrix obtained in the numerical simulations (red line). The curve is compared to that obtained by plotting the tensile stress in the cross-section of the bar elements, representing the fibers embedded in the composite, versus the above-defined number of cracks (blue line). The tensile stress is obtained by dividing the textile forces by the textile cross-section area. In particular, the tensile stress is evaluated in correspondence to a point near the joints where the hinge $H_2$ in Fig. 14 is supposed to open. In fact, as the matrix progressively cracks in that area, the opening of the hinge $H_2$ is hindered by the reinforcement, and tangential stresses developing at the CS interface are transferred to the bar elements through the matrix. Consequently, the tensile stress developing in the bars increases mostly in this range. Indeed, the tensile stress in the bar elements abruptly increases from 25 MPa to 135 MPa at point A, corresponding to a vertical load of 1776 N, and then up to 252 MPa at point B, corresponding to a vertical load of 1787 N. Subsequently, when the load transfer process between matrix and fiber net is completed, the axial forces in the bars progressively increase with the number of cracks, towards the final point C. Notice that here the tensile stress reach the value of 347 MPa, consistent with the debonding stress experimentally determined in [23].

On the red line in Fig. 15a, red dots mark the load values at which each hinge opens. In particular, the opening of hinges $H_1$ and $H_3$ is associated with a relative displacement in the direction normal to the interface cracks of 0.1 mm for the BB and CS interface. For detecting the opening of the hinge $H_2$, the load corresponding to the sudden increase of the axial forces in the reinforcing bar elements is considered. Finally, the formation of the hinge $H_4$ is identified by the cracking of the matrix and by a slight debonding of the reinforcement at the right abutment, which occurred practically simultaneously with the formation of $H_2$.

Comparing the diagram with the cracked configurations in Fig. 15b, it is easily seen that the progressive cracking of the composite corresponds to an increase in the axial forces developing in the bar elements. After the maximum load is reached, the number of cracks increases under a constant value of axial force in the reinforcement (before the sudden increase leading to point A in the blue curve in Fig. 15a). This means that the bond between the composite and the substrate is lost at the left abutment, and that the residual strength of the structure is substantially due to the fact that the reinforcement prevented the opening of hinge $H_2$ holding the bricks together. Notice that the cracking of the matrix starts before reaching the peak load, and evolves up to the collapse of the vault; therefore, it does not correspond to a particular point of the curves in Fig. 15a.

The above considerations allow showing that the proposed model is capable of successfully reproducing the stress-transfer mechanisms between the different components of the reinforced structure and its collapse mechanism.

### *6.2. Unreinforced vault (UV)*

Table 8 shows that for UV there is a small difference between the numerically estimated and experimentally evaluated collapse load (intended as the peak load). On the other hand, a quite large difference between experimental and numerical displacements of the loaded point at the peak load is observed. This discrepancy can be likely ascribed to the adopted experimental setup. In fact, experimental tests have been performed in load control that probably motivates the quite irregular trend of the experimental response characterized by the lack of the softening phase. Thus, the experimental peak load is coincident with the last recorded load value (correspondingly for the displacement). On the other hand, the numerical analysis allowed to capture the evolution of the softening phase.

About the numerical collapse mechanism for the UV, the typical four-hinge mechanism, also observed during the experiment, has been obtained. In particular, the first hinge $H_1$ appeared under the load application point, followed by the second hinge $H_2$ at the right abutment and the third hinge

$H_3$ at the left abutment. The collapse is reached when the fourth hinge $H_4$ opened at a symmetrical position with respect to $H_1$. The position of the hinges is visible in Fig. 16, where the relative displacements in the direction normal to the interface cracks are displayed in correspondence to the collapse load.

If the numerical collapse mechanism of the UV (see Fig. 16) is compared to the experimentally determined one (see Fig. 10), it can be noticed that the position of the hinges perfectly corresponds. However, it should be pointed out that the order of opening is slightly different; the hinge symmetrical to the load application point opens as the last in the numerical simulations, while it is the second to open in the experiments.

## 7. Sensitivity analysis

Parametric analyses are now performed to investigate the influence of each mechanical parameter required to describe the mechanical behaviour of the structure (masonry vault and FRCM composite) on the global response of the reinforced structure. For each analysis, only one of the mechanical parameters has been increased or decreased five times, while all the other parameters are kept constant.

The results of sensitivity analyses are discussed by grouping the investigated parameters. The discussion is eased using figures reporting the experimental data (dotted curve) the response obtained with the choice of the considered mechanical parameters reported in Section 5 (red curve), the response corresponding to the 5 times increased parameter (light blue curve), and the response corresponding to the 5 times decreased parameter (green curve). Possible relevant differences in the stress distribution or the collapse mechanism due to the variation of one of the mechanical parameters are highlighted.

### *7.1. BB interface*

Fig. 17 and Fig. 18a show the results in terms of load-displacement curves obtained from parametric analyses of the influence of the BB interface mechanical parameters on the global behaviour of the reinforced vault. Recall that the reference values are collected in Table 4.

The numerical results are mostly affected by the interface normal stiffness $k_{BBn}$ (Fig. 17a) and, secondarily, by the interface tensile strength $f_{mjt}$ (Fig. 18a). Indeed, 5 times increasing or decreasing of the interface tangent stiffness $k_{BBt}$ (Fig. 17b), the interface tensile fracture energy $G_{mjft}$ (Fig. 17c), or of the interface reduced shear modulus $G_{BB}$ (Fig. 17d) yield only negligible variations of the post-peak behaviour for higher displacements. In particular, lowering the interface normal stiffness $k_{BBn}$ corresponds to a significantly reduced stiffness of the vault and a considerably lower load carrying capacity, whereas increasing $k_{BBn}$ entails a small increase in the stiffness and the maximum load. This means that an error in excess in the evaluation of $k_{BBn}$ brings almost negligible effects, but too low $k_{BBn}$ values may lead to non-representative results.

The interface tensile strength $f_{mjt}$ could significantly influence the capacity of sustaining the load after the peak, see Fig. 18c. Indeed, whereas by lowering $f_{mjt}$ concerning the nominal value of 0.02 MPa small variations in the response (only in the immediately post-peak phase) are observed, whereas an error in excess for $f_{mjt}$ could yield a non-reasonable high post-peak load carrying capacity.

For explaining this large influence of the interface tensile strength $f_{mjt}$, notice that by assuming a 5 times higher value of $f_{mjt}$=0.1 MPa, the crack stresses configuration at the collapse in Fig. 18b reveals that the reinforcement does not completely debond from the substrate. On the contrary, debonding happens for the nominal value of $f_{mjt}$ (see Fig. 14b) and also for the 5 times lower value of $f_{mjt}$=0.004 MPa (Fig. 18c).

### *7.2. CS interface*

The efficiency of the reinforcement in improving the performance of the structure in terms of strength and ductility strongly depends on the bonding between the reinforcement FRCM composite and the substrate. This aspect is here investigated by parametric analyses by varying the mechanical properties of the CS interface.

The obtained load-displacement curves are shown in Fig. 19a - Fig. 20. It is seen that variations of the CS mechanical parameters mostly influence the post-peak behaviour, related to the debonding of the composite from the substrate at the left abutment.

Fig. 19a shows that the interface normal stiffness $k_{CSn}$ has a small influence on the response before the load peak, and also on the value of the load peak. After the peak, significant reductions of $k_{CSn}$ do not seem to influence the response, whereas too high values of $k_{CSn}$ might lead to a post-peak phase much more sustained than that experimentally observed. Moreover, for $k_{CSn}$=1500 N/mm$^3$, 5 times higher than the reference value, not only the reinforcement prevents the opening of a hinge near the left support, but also no debonding takes place from the substrate at the left end of the vault. Indeed, as shown in Fig. 19b, where the relative displacements in the direction normal to the interface cracks at the collapse are depicted, the debonding of the composite anchored on the left of the vault is observed. The above justifies the fact that for $k_{CSn}$=1500 N/mm$^3$ the vault deformations increase at an approximately constant load.

On the other hand, the interface tangential stiffness $k_{CSt}$ might influence more the first part of the response curve than the post-peak behaviour (see Fig. 20a). Specifically, a very low value of $k_{CSt}$ doesn't introduce substantial variations in the response, whereas an error in excess in the evaluation of $k_{CSt}$ leads to a stiffer response (the global stiffness of the reinforced vault raises from 747 N/mm to 1437 N/mm), although with no noticeable difference in the peak load and the post-peak phase. This behaviour is likely related to the fact that $k_{CSt}$=600 N/mm$^3$, 5 times the nominal value, reaches the same value of the normal stiffness $k_{CSn}$.

Moreover, even large variations of the interface tensile strength $f_{it}$ (Fig. 20c) result in a small variation of the peak load. In the post-peak phase, too low values of $f_{it}$ affect the response but in a limited and scarcely predictable way, whereas too high values of $f_{it}$ might yield to a sustained post-peak phase, due to the hindering of the debonding of the composite at the left abutment, and consequently to the induced delay in the collapse of the structure.

Errors in the determination of the interface tensile fracture energy $G_{ift}$ yield variations only in the post-peak behaviour (Fig. 20d), inducing a less or more fragile failure of the CS interface at the left abutment.

Finally, no appreciable changes are observed by varying 5 times the interface reduced shear modulus $G_{CS}$ (Fig. 20b), since the reference value is very low. It is necessary to introduce substantially higher values of $G_{CS}$ (yellow curve) to notice some variation of the response curve in the post-peak phase.

### *7.3.* FRCM *composite*

Here, the results obtained from the sensitivity analyses on the parameters ruling the mechanical behaviour of the FRCM composite are presented. The reference values of these parameters are collected in Table 6.

The load-displacement curves obtained by assuming the Young's modulus of the composite matrix $E_c$ equal to 32500 MPa and 1300 MPa, respectively, are compared in Fig. 21a to the curve obtained for nominal value $E_c$=6500 MPa. Recall that the latter is obtained by averaging the results of uniaxial tensile tests performed, referred to the first phase of the tests, when both the matrix and the textile are subjected to the load. It is easily seen that $E_c$ significantly affects the stiffness of the reinforced structure and, secondarily, the peak load and the post-peak behaviour. In particular, for $E_c$=1300 MPa the global stiffness is 40% reduced and the peak load decreases from 2204 N to 1995 N, whereas for $E_c$=32500 MPa the global stiffness is 30% increased, but the peak load undergoes a small increment, from 2204 N to 2224 N. Furthermore, it is possible to observe that higher FRCM Young's modulus yields a more sustained response after the peak, whereas lower values of $E_c$ result in a steeper drop of the load after the maximum.

Fig. 21b shows the response curves related to different values of the FRCM matrix tensile strength $f_{ct}$. This parameter significantly affects the numerical results. In particular, for $f_{ct}$=10.4 MPa (5 times the nominal value), after reaching a load of 2314 N, the composite partially detaches from the left abutment causing the load to decrease up to 2080 N. After that, the load starts increasing again and no cracks occurred in the matrix. On the contrary, for $f_{ct}$=0.4 MPa (20% of the nominal value), the structure reaches a much lower maximum load of 1830 N, and over 600 N the global stiffness is reduced due to the opening of the first hinge under the load application point. The collapse is due to the development of cracks all over the matrix and to the partial debonding of the composite from the left abutment. For the sake of completeness, it has to be noted that for $f_{ct}$=10.4 MPa, the deformation at the end of the elastic range $\varepsilon_{cu}$ considered in the JSCE model is 0.0016, greater than that considered in the calculations; therefore, the effects of tensile strength variations on the structural response of the reinforced vault could not be distinguished from that of the deformation $\varepsilon_{cu}$.

The JSCE model employed for the matrix in traction is characterized by a stress plateau after the appearance of the first cracks, followed by the exponential softening governed by the exponent *c* and by the deformation at the end of the stress plateau $\varepsilon_{cu}$. Possibly, the latter can be assumed equal to the deformation at the end of the elastic range; in this case, no stress plateau is obtained. In particular, Fig. 22b shows the curves corresponding to the JSCE tension model (6) for different values of $\varepsilon_{cu}$ and fixed exponent *c*; these curves tend to approach zero stress only for very high values of strain, providing for the residual tensile strength characterizing FRCM composites. The effects of variations in the exponent *c* on the constitutive response of FRCM in tension are outlined in Fig. 22d for fixed $\varepsilon_{cu}$=0.00032. The parameter *c* affects the area under the response curve; in particular, higher values of c reduce this area and consequently the tensile fracture energy, leading to a more fragile behaviour.

Fig. 22a shows the numerical response curves obtained for different values of $\varepsilon_{cu}$. In this case, no lower values than the nominal one ($\varepsilon_{cu}=f_{cc}/E_c$=0.00032) are considered, to avoid inconsistency with the value of the Young's modulus $E_c$ and/or of the compressive strength $f_{cc}$. Changes in $\varepsilon_{cu}$ result in appreciable variations in the response for high deformations; in particular, for $\varepsilon_{cu}$=0.0016, 5 times the nominal value, a much more sustained post-peak behaviour is obtained.

The effects of variations of the exponent *c* on the global behaviour of the reinforced vault are shown in Fig. 22c. For *c* equal to 0.2 (light blue curve), a value usually considered for reinforced concrete, after the peak the load remains almost constant, while for *c*=0.8 (green curve) the load-displacement curve is only marginally different from that corresponding to the nominal value *c*=0.4. Anyway, it is worth noting that the curve obtained for *c*=0.8 better approximates the experimental curve in the post-peak phase.

As for variations of the compressive strength of the cementitious matrix $f_{cc}$ (see Fig. 23a), for $f_{cc}$=37.4 MPa, five times higher than the nominal value, the maximum load remains the same, but the global stiffness is almost doubled, while assuming $f_{cc}$=1.496 MPa (20% of the nominal value), the peak load and the stiffness are slightly lowered. Assuming too low values of the compressive fracture energy $G_{cc}$ does not seem to hold a significant influence on the mechanical behaviour of the reinforced vault. In fact, if $G_{cc}$ is decreased five times, the load-displacement curve (green curve in Fig. 23b) is practically superimposed to that obtained for the nominal value $G_{cc}$=11.97 N/mm. On the other hand, if $G_{cc}$ is increased five times, the obtained peak load is higher than the experimental value, and convergence problems occurred (light blue curve in Fig. 23b).

Finally, parametric analyses are performed on the elastic properties and the tensile strength of the fibers. It is worth recalling that the average tensile stress-strain response experimentally determined in [23] and corresponding to the average curve in Fig. 11 (in blue) is implemented for the bars, with the following reference values: Young's modulus $E_f$=78.9 GPa and tensile strength $f_{ft}$=529.16 MPa.

Fig. 24a shows the effect of variations of the Young's modulus $E_f$ of the fibers, resulting in relatively small changes in the peak load and the post-peak behaviour. Variations of the tensile strength of the fibers $f_{ft}$ (see Fig. 24b) yields even smaller variations of load carrying capacity and of the softening branch of the load-displacement curve.

### *7.4. Masonry bricks*

For reinforced masonry arches and vaults, the mechanical properties defining the substrate inelastic behaviour in tension (tensile strength and tensile fracture energy) and in compression (compressive strength and compressive fracture energy) can play an important role in describing the load capacity of the whole structure. Indeed, the reinforcement prevents hinge openings at some of the block-joint interfaces and the rotation of the blocks; this yields much higher tensile and compressive stresses in the blocks with respect to what happens for unreinforced structures. This is illustrated in Fig. 25, where the maximum principal stresses are plotted for the unreinforced and reinforced vaults. In particular, the figure displays the detail of the part of the vault where the hinge labelled H2 opens; the same colour scale for stresses is employed (from 0 to 0.8 MPa). In the case of the reinforced vault, results for $f_{bt}$=0.8 MPa (the nominal value) and for $f_{bt}$=4 MPa are reported (see Fig. 25b and c). It is evident that the reinforcement system prevents the opening of joints, and this leads to the development of higher tensile stresses in the bricks.

As a consequence, by varying $f_{bt}$ while all the other mechanical parameters being fixed, very different load-displacement curves are obtained, see Fig. 27a. In particular, when the bricks tensile strength is increased five times ($f_{bt}$=4 MPa) the load-displacement curve does not show any softening phase, and the collapse is obtained for a much higher load, due to the cracking of the matrix, no longer able to transfer the stresses from the substrate to the fiber mesh (see also Fig. 26). If the reference $f_{bt}$ is reduced five times, a sudden decrease of the stiffness is noted after a load value of 1088 N, with a slight change in the peak load and no appreciable variations in the post-peak phase.

Fig. 27c shows that also changes in the brick tensile fracture energy $G_{bft}$ could lead to evident variations in the response curve. Indeed, an increase or decrease of the load carrying capacity of the structure of about 30% when $G_{bft}$ is respectively increased or decreased five times is obtained. Thus, it emerges that numerical results are strongly affected by the tensile strength and the tensile fracture energy of the substrate material. On the contrary, the compressive fracture energy $G_{bc}$ does not influence at all the mechanical behaviour of the strengthened structure since the three curves obtained for the different considered values of $G_{bc}$ are completely superimposed; thus, for the sake of brevity, these load-displacement curves have not been reported.

Furthermore, it is interesting to observe that an increase in the brick's compressive strength $f_{bc}$ affects the global stiffness of the vault. In fact, the blue curve in Fig. 27b, corresponding to $f_{bc}$=53.5 MPa (five times the reference value $f_{bc}$=10.7 MPa), is characterized by a higher stiffness than the reference curve. The latter is very close to the curve obtained for the lower value of $f_{bc}$. No noticeable changes in the peak load or the post-peak behaviour are observed by changing $f_{bc}$.

Finally, Fig. 27d describes the effect of variations of bricks Young's modulus $E_b$. It is seen that this parameter greatly influences the overall stiffness, the peak load and also the post-peak behaviour. Thus, for the numerical model to be representative, the Young's modulus of the bricks has to be carefully characterized [53].

### *7.5. Concluding remarks*

The performed sensitivity analyses suggest that stiffness parameters (interface stiffness and elastic moduli) can be even more influential than strength parameters. This is likely because large variations in the stiffness of one of the components of the structural model could radically vary the stress transfer arrangements, thus activating or completely deactivating some collapse mechanisms. On the other hand, large variations in strength parameters are influent only if the related failure is active, and to the extent to which that failure contributes to the overall behaviour and to which that parameter has been varied. The highly non-linear behaviour of reinforced masonry arches and vaults and the possibility of several different stress transfer and internal failure mechanisms render rather unpredictable the effects of variations of more than one mechanical parameter, with possible unrealistic numerically simulated results.

The above considerations, however, should not obscure the most important result of Section 7, namely that the proposed numerical modelling strategy is capable of giving representative results, satisfactorily close to the actual structural response, provided that mechanical parameters are reasonably estimated. In particular, the model is quite robust concerning small errors in the determination of mechanical parameters, apart from some of them that can be easily and suitably evaluated by standard mechanical tests. Moreover, the sensitivity analyses indicate those parameters that can be determined by a rough estimate, and those needing to be carefully determined for the accuracy of the simulated behaviour.

In particular, for the BB interface, a correct estimation of the normal stiffness is required. Since this parameter is difficult to be experimentally characterized, it is possible to determine it by eq. (7). Thus, an accurate experimental determination of the Young's moduli of the bricks, the mortar, and the average thickness of masonry joints is needed. For the tensile strength of the BB interface, only a large overestimating error could secondarily affect the results in the post-peak phase. Other BB interface parameters scarcely influence the overall response of the reinforced vault.

A correct determination of the parameters characterizing the CS interface appears to be a little more influential on the overall response reconstruction. In particular, a large overestimation of the normal stiffness or the tangent stiffness could lead to unrealistic stiffness and post-peak behaviour. These stiffnesses are very difficult to identify by experimental tests; thus, the suggestion is to use eq. (7) and carefully evaluating by experimental tests the Young's moduli of the bricks and the reinforcing mortar. The tensile strength of the CS interface can be experimentally determined, but large errors influence practically only the post-peak behaviour. The same occurs for the CS tensile fracture energy.

Some mechanical parameters of the FRCM composite show a pronounced influence on the numerical results. However, the most influential parameters can be accurately determined by standard mechanical tests. In particular, this is true for the Young's modulus of the matrix, the composite tensile strength, the composite tensile strain at the end of the stress plateau, and the FRCM compressive strength. For what concerns the exponent c, also influent on the post-peak response, the value suggested by the literature allows for reasonable results.

Finally, the numerically predicted response could be markedly influenced by large variations of masonry bricks mechanical parameters, with special reference to the Young's modulus $E_b$, the tensile strength $f_{bt}$ and the tensile fracture energy $G_{bft}$. However, $E_b$ and $f_{bt}$ can be directly determined employing ordinary mechanical tests, whereas the determination of the tensile fracture energy can be based on the literature. Also the masonry bricks compressive strength, affecting the initial stiffness, can be easily evaluated by standard mechanical tests.

# 8. Pushover curves

As discussed in Section 6, the numerical model presented in Sections 3-5 gives results quite similar to the experimental ones reported in [23] in terms of load-displacement curve, peak load and displacement of the application point of the load in correspondence of the peak load. This is obtained by using mechanical parameters experimentally determined or evaluated according to the literature, without any calibration based on the (unknown in advance for practical applications) experimental response.

Thus, this numerical model can be considered representative of the actual structural behaviour and can be used to perform other kinds of structural analyses. In particular, here a pushover analysis aimed at determining the maximum seismic capacity in terms of horizontal ground acceleration for the examined vaults is performed, studying the influence of the FRCM strengthening system [54].

The pushover analysis is carried out by applying first the self-weight and then a system of horizontal forces proportional to the self-weight monotonically increased from zero in steps of suitable amplitude. One node at the centre of the keystone is assumed as the control point for determining the capacity curve.

In particular, Fig. 28 shows the capacity curves for the unstrengthened (UV) and the reinforced vault (RV) in terms of the base shear force normalized to the self-weight of the structure $\lambda$ versus displacement of the selected control point. Notice that $\lambda$ can be interpreted as the base horizontal acceleration in g. Moreover, the deformed configuration of the reinforced vault at collapse is shown and the interface relative displacements DUNy are plotted.

Since for the examined load conditions no experimental results are available, for the validation of the numerical results the maximum horizontal load numerically determined for the unstrengthened vault (UV) is compared to that evaluated by applying the kinematic theorem of Limit Analysis. In particular, the latter provided a collapse horizontal load multiplier $\lambda_k$=1.03, which can be considered consistent with the collapse horizontal load multiplier $\lambda$=1.031 numerically evaluated through the pushover analysis.

The pushover analysis performed for the reinforced vault (RV) yields a horizontal loads multiplier at the collapse $\lambda$=4.11, about 4 times higher than that obtained for the unstrengthened vault. As the capacity curves in Fig. 28 show, the reinforcement strongly reduces the lateral displacements of the structure, while increasing the load carrying capacity under horizontal loads. On the other hand, the unreinforced vault is capable of quite larger horizontal displacements under an almost constant load.

In Fig. 29 the stresses developing in the reinforcement bar during the pushover analysis are plotted and related to the position where each mesh element of the bar is positioned along the span; the plotted curves correspond to different values of $\lambda$: 1.03, which is the collapse multiplier of the unreinforced vault, 2.00, when the first hinge opens, 2.80, when the first cracks occur, 4.11 and 3.60 which correspond to the maximum value and the last recorded value, respectively. In the same picture the crack pattern at collapse ($\lambda$=3.60) has been reported and scaled to approximately fit the span length.

Starting from a value of $\lambda$=2.00, at almost a quarter of the span, one of the bricks started to slightly separate from the contiguous blocks, as shown in Fig. 28 in the part of the vault marked with a red circle, and the interface relative displacements at the intrados grew from 0.11 mm up to 0.35 mm, when the maximum value of $\lambda$ (4.11) was reached.

At $\lambda$=2.8 the first cracks occurred at the left abutment, spreading through the block towards the reinforcement. As the load was increasing, the relative displacements at the CS interface started to grow both normally to the interfaces and, with less intensity, tangent to the interfaces. From the curves plotted in Fig. 29 it can be observed that in some parts of the composite, the stresses developing in the reinforcement bar are very low, while the stresses increase, as the load grow, near the abutment and in proximity to the part where the first hinge occurred, that is in those parts of the vaults where the bond at the composite-substrate interface weakened. At collapse, the stresses in the textile reach their peak and, contextually, the reinforcement detached almost completely from the left abutment, causing the failure of the vault.

# 9. Conclusions

The present paper proposes a new modelling strategy for masonry curved structures reinforced with FRCM composites, suitable for its use by practitioners in advanced commercial codes, like the finite element code DIANA FEA here used.

The modelling strategy here proposed combines the advantages of both macro- and micro-modelling approaches. In particular, in the frame of a macro-modelling approach, the reinforcement is described as a continuum whose mechanical properties are the ones of the whole composite itself; a smeared cracking constitutive model is considered to reproduce the occurrence of cracks in the matrix in the areas where the reinforcement prevents the opening of the hinges in the structure. The presence of the fibers net is represented by means of bars embedded in the continuum without interfaces ruling the contact between the two. All the other interactions between materials are described by a suitable interface model, as it is typical of micro-models. The above approach brings the advantage of reducing the number of mechanical parameters to be determined, along with the number of interfaces elements involved in the model, with benefit in terms of computational costs. Each of the analyses performed required less than 1 hour to be performed on a standard notebook.

For the validation of the proposed approach, a case study taken from the recent literature has been considered. Particular attention has been devoted to a suitable choice of the mechanical parameters that could not be determined by experimental tests, and have to be evaluated indirectly by employing literature formulations.

The comparison between the results obtained from the numerical model and the available experimental response showed the accuracy of the proposed approach in reproducing the load carrying capacity of the examined curved structure also in the post-peak branch of the load-displacement curve. In addition, the mechanisms ruling the collapse have been correctly represented, especially with reference to the cracking of the composite and the stress transfer mechanisms. It can be inferred that the effects of the curvature on the complex phenomena involved in the structural behaviour of the FRCM reinforced vault has been correctly represented. Notice that if at first glance it might emerge a small inconsistency with the initial stiffness, the latter is likely due to the structure settling in the reference experiment, and therefore it is possible to say that the proposed model is capable of recovering the more relevant aspects of the observed structural behavior. Moreover, it should be remarked that the material parameters have not been selected fitting the results of the experimental curve, but based on available data of the materials.

The large sensitivity analysis shows the influence of variations of the mechanical parameters on the predicted overall response of the reinforced structure. It emerges that for some parameters even large inaccuracies in their determination marginally affect the result, whereas other parameters need to be accurately identified to generate representative results. These considerations might be very useful in practical applications to guide choices on the experimental analyses to be performed and the criteria to be followed for accurately reproducing the actual structural behaviour.

Once the proposed numerical model has been validated with respect to the experimental data, the influence of the FRCM reinforcement on the seismic capacity of the structure has been investigated by performing pushover analyses both on the unstrengthened and strengthened vault.

The obtained results suggest that the proposed modelling approach could represent a useful compromise between the accuracy of the results and the feasibility for use in practical applications. This is very interesting for the still open research field of the mechanics of FRCM reinforced masonry arches and vaults. A further appealing aspect is that the proposed modelling strategy requires for the mechanical parameters of the masonry and the reinforcement a knowledge level readily achievable with standard experimental approaches.

**Acknowledgment and Compliance with Ethical Standards**

Funding: Financial support from ReLUIS (Italian Department of Civil Protection) and from the Italian Ministry of University and Research (MUR) in the framework of Project PRIN2020 #20209F3A37 is gratefully acknowledged.

Conflict of Interest: The authors declare that they have no conflict of interest.

## 10. References

[1] C. Wang, V. Sarhosis, N. Nikitas, Strengthening/Retrofitting Techniques on Unreinforced Masonry Structure/Element Subjected to Seismic Loads: A Literature Review, The Open Construction and Building Technology Journal. (2018). https://doi.org/10.2174/1874836801812010251.

[2] G. de Felice, S. de Santis, L. Garmendia, B. Ghiassi, P. Larrinaga, P.B. Lourenço, D. v. Oliveira, F. Paolacci, C.G. Papanicolaou, Mortar-based systems for externally bonded strengthening of masonry, Materials and Structures/Materiaux et Constructions. 47 (2014) 2021–2037. https://doi.org/10.1617/s11527-014-0360-1.

[3] I. Mascolo, A. Fortunato, C. Olivieri, A. Gesualdo, Seismic retrofitting techniques for existing masonry buildings, COMPDYN Proceedings. 2021-June (2021). https://doi.org/10.7712/120121.8514.19628.

[4] C. Caggegi, F.G. Carozzi, S. De Santis, F. Fabbrocino, F. Focacci, Ł. Hojdys, E. Lanoye, L. Zuccarino, Experimental analysis on tensile and bond properties of PBO and aramid fabric reinforced cementitious matrix for strengthening masonry structures, Compos B Eng. 127 (2017) 175–195. https://doi.org/10.1016/j.compositesb.2017.05.048.

[5] C.A. Filippou, C.Z. Chrysostomou, Analytical model for textile reinforced mortar under monotonic loading, Constr Build Mater. 258 (2020) 120178. https://doi.org/10.1016/J.CONBUILDMAT.2020.120178.

[6] E. Grande, G. Milani, M. Imbimbo, Theoretical model for the study of the tensile behavior of FRCM reinforcements, Constr Build Mater. 236 (2020) 117617. https://doi.org/10.1016/J.CONBUILDMAT.2019.117617.

[7] J. Donnini, V. Corinaldesi, A. Nanni, Mechanical properties of FRCM using carbon fabrics with different coating treatments, Compos B Eng. 88 (2016) 220–228. https://doi.org/10.1016/j.compositesb.2015.11.012.

[8] F. Nerilli, S. Marfia, E. Sacco, Micromechanical modeling of the constitutive response of FRCM composites, Constr Build Mater. (2020). https://doi.org/10.1016/j.conbuildmat.2019.117539.

[9] A. Razavizadeh, B. Ghiassi, D. V. Oliveira, Bond behavior of SRG-strengthened masonry units: Testing and numerical modeling, Constr Build Mater. 64 (2014) 387–397. https://doi.org/10.1016/j.conbuildmat.2014.04.070.

[10] E. Grande, M. Imbimbo, E. Sacco, Investigation on the bond behavior of clay bricks reinforced with SRP and SRG strengthening systems, Materials and Structures/Materiaux et Constructions. 48 (2015) 3755–3770. https://doi.org/10.1617/s11527-014-0437-x.

[11] R. Allahvirdizadeh, D. v. Oliveira, R.A. Silva, Numerical modeling of the seismic out-of-plane response of a plain and TRM-strengthened rammed earth subassembly, Eng Struct. 193 (2019) 43–56. https://doi.org/10.1016/j.engstruct.2019.05.022.

[12] C. D'Ambra, G.P. Lignola, A. Prota, F. Fabbrocino, E. Sacco, FRCM strengthening of clay brick walls for out of plane loads, Compos B Eng. 174 (2019) 107050. https://doi.org/10.1016/j.compositesb.2019.107050.

[13] J. Scacco, B. Ghiassi, G. Milani, P.B. Lourenço, A fast modeling approach for numerical analysis of unreinforced and FRCM reinforced masonry walls under out-of-plane loading, Compos B Eng. 180 (2020) 107553. https://doi.org/10.1016/j.compositesb.2019.107553.

[14] X. Wang, B. Ghiassi, D. v. Oliveira, C.C. Lam, Modelling the nonlinear behaviour of masonry walls strengthened with textile reinforced mortars, Eng Struct. 134 (2017) 11–24. https://doi.org/10.1016/j.engstruct.2016.12.029.

[15] M. Saidi, A. Gabor, Adaptation of the strain measurement in textile reinforced cementitious matrix composites by distributed optical fibre and 2D digital image correlation, Strain. 56 (2020) e12335. https://doi.org/10.1111/STR.12335.

[16] E. Bertolesi, M. Fagone, T. Rotunno, E. Grande, G. Milani, Experimental characterization of the textile-to-mortar bond through distributed optical sensors, Constr Build Mater. 326 (2022) 126640. https://doi.org/10.1016/J.CONBUILDMAT.2022.126640.

[17] E. Cescatti, F. da Porto, C. Modena, In-Situ Destructive Testing of Ancient Strengthened Masonry Vaults, International Journal of Architectural Heritage. 12 (2018) 350–361. https://doi.org/10.1080/15583058.2017.1323243.

[18] A. Borri, G. Castori, M. Corradi, Intrados strengthening of brick masonry arches with composite materials, Compos B Eng. 42 (2011) 1164–1172. https://doi.org/10.1016/j.compositesb.2011.03.005.

[19] L. Garmendia, I. Marcos, E. Garbin, M.R. Valluzzi, Strengthening of masonry arches with Textile-Reinforced Mortar: experimental behaviour and analytical approaches, Materials and Structures/Materiaux et Constructions. 47 (2014) 2067–2080. https://doi.org/10.1617/s11527-014-0339-y.

[20] A. Castellano, A. Fraddosio, J. Scacco, G. Milani, M.D. Piccioni, Dynamic Response of FRCM Reinforced Masonry Arches, Key Eng Mater. 817 (2019) 285–292. https://doi.org/10.4028/www.scientific.net/kem.817.285.

[21] I. Boem, N. Gattesco, Cyclic behavior of masonry barrel vaults strengthened through Composite Reinforced Mortar, considering the role of the connection with the abutments, Eng

Struct. 228/2021 (2021). https://doi.org/10.1016/J.ENGSTRUCT.2020.111518.

[22] R. Varró, G. Bögöly, P. Görög, Laboratory and numerical analysis of failure of stone masonry arches with and without reinforcement, Eng Fail Anal. 123 (2021) 105272. https://doi.org/10.1016/J.ENGFAILANAL.2021.105272.

[23] F.G. Carozzi, C. Poggi, E. Bertolesi, G. Milani, Ancient masonry arches and vaults strengthened with TRM, SRG and FRP composites: Experimental evaluation, Compos Struct. 187 (2018) 466–480. https://doi.org/10.1016/j.compstruct.2017.12.075.

[24] M. Malena, G. de Felice, Debonding of composites on a curved masonry substrate: Experimental results and analytical formulation, Compos Struct. 112 (2014) 194–206. https://doi.org/10.1016/j.compstruct.2014.02.004.

[25] V. Alecci, G. Misseri, L. Rovero, G. Stipo, M. de Stefano, L. Feo, R. Luciano, Experimental investigation on masonry arches strengthened with PBO-FRCM composite, Compos B Eng. (2016). https://doi.org/10.1016/j.compositesb.2016.05.063.

[26] S. de Santis, F. Roscini, G. de Felice, Full-scale tests on masonry vaults strengthened with Steel Reinforced Grout, Compos B Eng. 141 (2018) 20–36. https://doi.org/10.1016/j.compositesb.2017.12.023.

[27] A. Borri, P. Casadei, G. Castori, J. Hammond, Strengthening of Brick Masonry Arches with Externally Bonded Steel Reinforced Composites, Journal of Composites for Construction. 13 (2009) 468–475. https://doi.org/10.1061/(asce)cc.1943-5614.0000030.

[28] B. Pantò, M. Malena, G. de Felice, A macro-modelling approach for arches strengthened with externally bonded inorganic matrix composites, Structures. 33 (2021) 4299–4312. https://doi.org/10.1016/J.ISTRUC.2021.07.015.

[29] E. Bertolesi, F.G. Carozzi, G. Milani, C. Poggi, Masonry arches retrofitted with steel reinforced grout materials: In-situ experimental tests and advanced FE simulations, AIP Conf Proc. 1906 (2017). https://doi.org/10.1063/1.5012361.

[30] E. Ricci, D. v. Oliveira, E. Sacco, B. Ghiassi, Modelling of masonry arches strengthened at extrados with FRCM, in: Proceedings of the International Masonry Society Conferences, International Masonry Society, Milan, 2018: pp. 2150–2162.

[31] P. Zampieri, Horizontal capacity of single-span masonry bridges with intrados FRCM strengthening, Compos Struct. 244 (2020). https://doi.org/10.1016/j.compstruct.2020.112238.

[32] E. Bertolesi, G. Milani, J. Adam, P. Calderón, 3D advanced numerical modelling of a catalan-layered masonry vault unreinforced and reinforced with glass-TRM materials and subjected to vertical support movements, COMPDYN Proceedings. 2021-June (2021). https://doi.org/10.7712/120121.8495.19253.

[33] S. de Santis, F.G. Carozzi, G. de Felice, C. Poggi, Test methods for Textile Reinforced Mortar systems, Compos B Eng. 127 (2017) 121–132. https://doi.org/10.1016/j.compositesb.2017.03.016.

[34] F. Focacci, T. D’Antino, C. Carloni, Tensile Testing of FRCM Coupons for Material Characterization: Discussion of Critical Aspects, Journal of Composites for Construction. 26 (2022) 04022039. https://doi.org/10.1061/(ASCE)CC.1943-5614.0001223.

[35] P.B. Lourenço, Computational strategies for masonry structures, Doctoral Dissertation, Delft University of Technology, 1996. http://resolver.tudelft.nl/uuid:4f5a2c6c-d5b7-4043-9d06-8c0b7b9f1f6f.

[36] R.G. Selby, F.J. Vecchio, Three-dimensional Constitutive Relations for Reinforced Concrete. Tech. Rep. 93-02, 1993.

[37] P.H. Feenstra, Computational aspects of biaxial stress in plain and reinforced concrete, Delft University of Technology, 1993.

[38] J.G. Rots, Computational modeling of concrete fracture, 1988. http://resolver.tudelft.nl/uuid:06985d0d-1230-4a08-924a-2553a171f08f.

[39] H.P. Backes, Tensile strength of masonry, in: Proceedings of the 7th International Brick Maonry Conference, 1985: pp. 779–790.

[40] D.A. Hordijk, Local approach to fatigue of concrete, 1991.

[41] Japan Society of Civil Engineers (JSCE), STANDARD SPECIFICATIONS FOR CONCRETE STRUCTURES - 2007 “Materials and Construction,” 2007.

[42] P.B. Lourenço, Computational strategies for masonry structures, Delft University of Technology, 1996. https://doi.org/ISBN 90-407-1221-2.

[43] L. Bejarano-Urrego, E. Verstrynge, G. Giardina, K. Van Balen, Crack growth in masonry: Numerical analysis and sensitivity study for discrete and smeared crack modelling, Eng Struct. 165 (2018) 471–485. https://doi.org/10.1016/j.engstruct.2018.03.030.

[44] L. Macorini, B.A. Izzuddin, A non-linear interface element for 3D mesoscale analysis of brick-masonry structures, Int J Numer Methods Eng. 85 (2011) 1584–1608. https://doi.org/10.1002/nme.3046.

[45] P.B. Lourenço, Analysis of masonry structures with interface elements, Comput Mech. (1994) 34.

[46] A. Gesualdo, G. Brandonisio, A. De-Luca, A. Iannuzzo, A. Montanino, C. Olivieri, Limit analysis of cloister vaults: The case study of Palazzo Caracciolo di Avellino, J Mech Mater Struct. (2019). https://doi.org/10.2140/jomms.2019.14.739.

[47] E. Bertolesi, G. Milani, F.G. Carozzi, C. Poggi, Ancient masonry arches and vaults strengthened with TRM, SRG and FRP composites: Numerical analyses, Compos Struct. 187 (2018) 385–402. https://doi.org/10.1016/j.compstruct.2017.12.021.

[48] P.B. Lourenço, A user/programmer guide for the micro-modelling of masonry structures, Delft, 1996.

[49] STANDARD SPECIFICATIONS FOR CONCRETE STRUCTURES – 2007 “Design” Japan Society of Civil Engineers, (n.d.).

[50] C. CEB-FIP, Model Code 1990, Comite Euro-International Du Beton, Paris. (1991) 87–109.

[51] E. Grande, G. Milani, E. Sacco, Modelling and analysis of FRP-strengthened masonry panels, Eng Struct. 30 (2008) 1842–1860. https://doi.org/10.1016/j.engstruct.2007.12.007.

[52] M. Angelillo, P.B. Lourenço, G. Milani, Masonry behaviour and modelling, in: CISM International Centre for Mechanical Sciences, Courses and Lectures, 2014: pp. 1–26. https://doi.org/10.1007/978-3-7091-1774-3_1.

[53] R. Quinteros-Mayne, I. de Arteaga, R. Goñi-Lasheras, A. Villarino, J.I. Villarino, The influence of the elastic modulus on the finite element structural analysis of masonry arches, Constr Build Mater. (2019). https://doi.org/10.1016/j.conbuildmat.2019.06.013.

[54] N. Ademović, M. Hadzima-Nyarko, G. Pavić, Modern Strengthening Methods for URM, in: Sustainability and Automation in Smart Constructions, 2021: pp. 357–362. https://doi.org/10.1007/978-3-030-35533-3_43.

# 10. List of tables

**Table 1. Matrix-bar (MB) interface mechanical parameters.**

| MB | Normal Stiffness $k_n$ [N/mm$^3$] | Shear stiffness $k_s$ [N/mm$^3$] | Tensile strength $f_t$ [N/mm$^2$] | Tensile fracture energy $G_{ft}$ [N/mm] | Reduced shear modulus $G_{MB}$ [N/mm$^2$] |
|---|---|---|---|---|---|
| | 5000.0 | 2000.0 | 3 | 1.5 | 1 |

**Table 2. Geometrical data for the vault.**

| Center | Thickness [mm] | Width [mm] | Span [mm] | Rise [mm] | Mid-line radius [mm] |
|---|---|---|---|---|---|
| C(0, -1164.98) | 60 | 300 | 2555 | 461 | 2025 |

**Table 3. Experimental data on the mechanical properties of materials** [23]**.**

| Test | n. sample | Data | | |
|---|---|---|---|---|
| Compressive test on bricks | 8 | Young's modulus | $E_b$ | 2016 MPa |
| | | Compressive strength | $f_{bc}$ | 10.7 MPa |
| Brazilian test on bricks | n.a. | Tensile strength | $f_{bt}$ | 0.8 MPa |
| Compressive test on masonry | 1 | Mortar Young's modulus | $E_{mj}$ | 306/337 MPa |
| | | Compressive strength | $f_{mjc}$ | 3.5 MPa |
| Tensile test on dry glass fibers | 5 | Weight per unit area | $\rho_f$ | 223.4 kg/m$^2$ |
| | | Young's modulus | $E_f$ | 75.43 GPa |
| | | Tensile strength | $f_{ft}$ | 1.442 GPa |
| Three-point bending test on lime mortar for FRCM composite | n.a. | Young's modulus | $E_{lm}$ | 6080 MPa |
| | | Compressive strength | $f_{lmc}$ | 7.48 MPa |
| | | Flexural strength | $f_{lmt,b}$ | 3.16 MPa |
| Pull-off test on FRCM composite | 3 | Maximum bond stress | | |
| | | Reinforcement applied to the brick | $\sigma_{bd}$ | 0.17 MPa |
| | | Reinforcement applied to both brick and mortar joint | $\sigma_{bd}$ | 0.05 MPa |
| Shear test on FRCM composite | 5 | Debonding stress | $\sigma_{sd}$ | 335 MPa |
| Tensile test on FRCM composite | n.a. | Trilinear stress-strain curve | (see Fig. 11) | |

**Table 4. BB interface mechanical parameters.**

| BB | Normal Stiffness | Tangent stiffness | Tensile strength | Tensile fracture energy | Reduced shear modulus |
|---|---|---|---|---|---|
| | $k_{BBn}$ | $k_{BBt}$ | $f_{mjt}$ | $G_{mjft}$ | $G_{BB}$ |
| | [N/mm$^3$] | [N/mm$^3$] | [MPa] | [N/mm] | [MPa] |
| | 38.25 | 15.3 | 0.02 | 0.012 | 0.01 |

**Table 5. CS interface mechanical parameters.**

| CS | Normal Stiffness | Tangent stiffness | Tensile strength | Tensile fracture energy | Reduced shear modulus |
|---|---|---|---|---|---|
| | $k_{CSn}$ | $k_{CSt}$ | $f_{it}$ | $G_{ift}$ | $G_{CS}$ |
| | [N/mm$^3$] | [N/mm$^3$] | [MPa] | [N/mm] | [MPa] |
| | 300.0 | 120.0 | 0.05 | 0.0072 | 0.01 |

**Table 6. FRCM composite mechanical parameters (Total Strain Rotating Crack model).**

| Young's modulus | Poisson's ratio | Mass density | Tensile strength | Tensile strain at the end of the plateau | Power exponent | Compressive strength | Compressive fracture energy |
|---|---|---|---|---|---|---|---|
| $E_c$ | $\nu_c$ | $\rho_c$ | $f_{ct}$ | $\varepsilon_{cu}$ | $c$ | $f_{cc}$ | $G_{cc}$ |
| [GPa] | [-] | [kg/m$^3$] | [MPa] | [-] | [-] | [MPa] | [N/mm] |
| 6500 | 0.2 | 1900 | 2.08 | 0.00032 | 0.4 | 7.48 | 11.97 |

**Table 7. Masonry bricks mechanical parameters.**

| Young's modulus | Poisson's ratio | Mass density | Compressive strength | Compressive fracture energy | Tensile strength | Tensile fracture energy |
|---|---|---|---|---|---|---|
| $E_b$ | $\nu_b$ | $\rho_b$ | $f_{bc}$ | $G_{bc}$ | $f_{bt}$ | $G_{bft}$ |
| [MPa] | [-] | [kg/m$^3$] | [MPa] | [N/mm] | [MPa] | [N/mm] |
| 2016 | 0.2 | 1800 | 10.7 | 17.12 | 0.8 | 0.0232 |

**Table 8. Comparison between the numerical and experimental results.**

| | $UV_{EXP}$ | $UV_{NUM}$ | $RV_{EXP}$ | $RV_{NUM\_1}$ | $RV_{NUM\_2}$ |
|---|---|---|---|---|---|
| **Collapse load** $F_{max}$ [N] | 390 | 380 | 2170 | 2204 | 2212 |
| **Displacement of the loaded point at the collapse load** $\delta_{max}$ [mm] | 6.41 | 1.54 | 4.08 | 3.43 | 3.74 |

# 11. List of figures

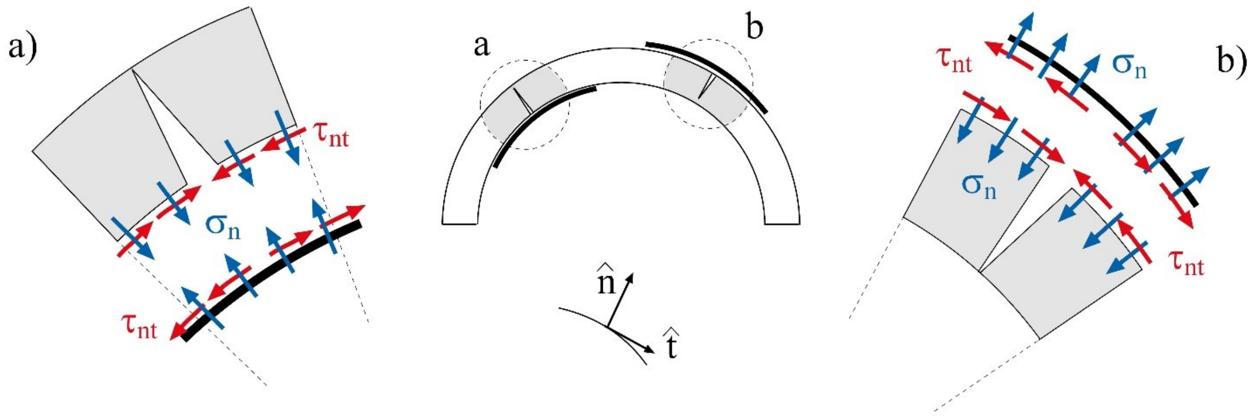


**Fig. 1. Stress transfer between the arch/vault and reinforcements applied at the intrados (a) or extrados (b).**

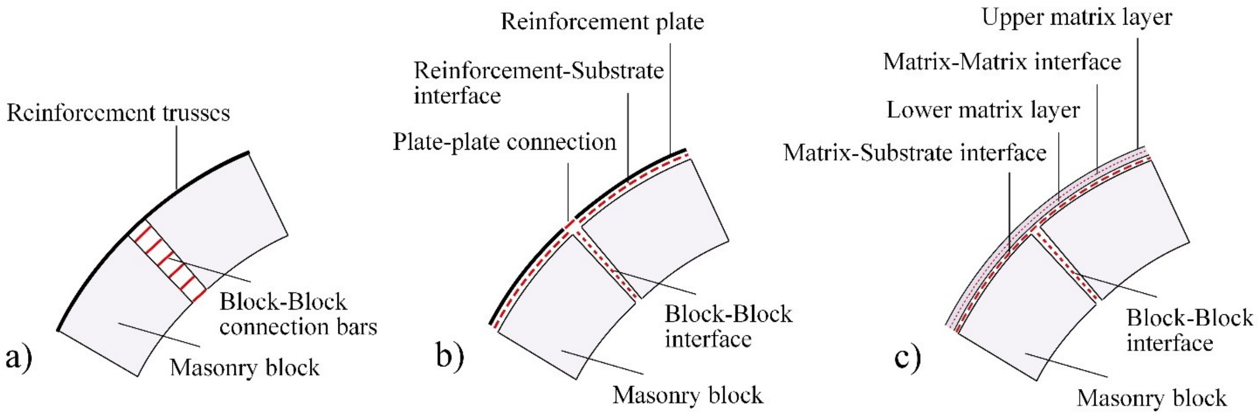


**Fig. 2. Numerical approaches in literature for FRCM reinforced arches: (a)** [31], **(b)** [36], **(c)** [32].

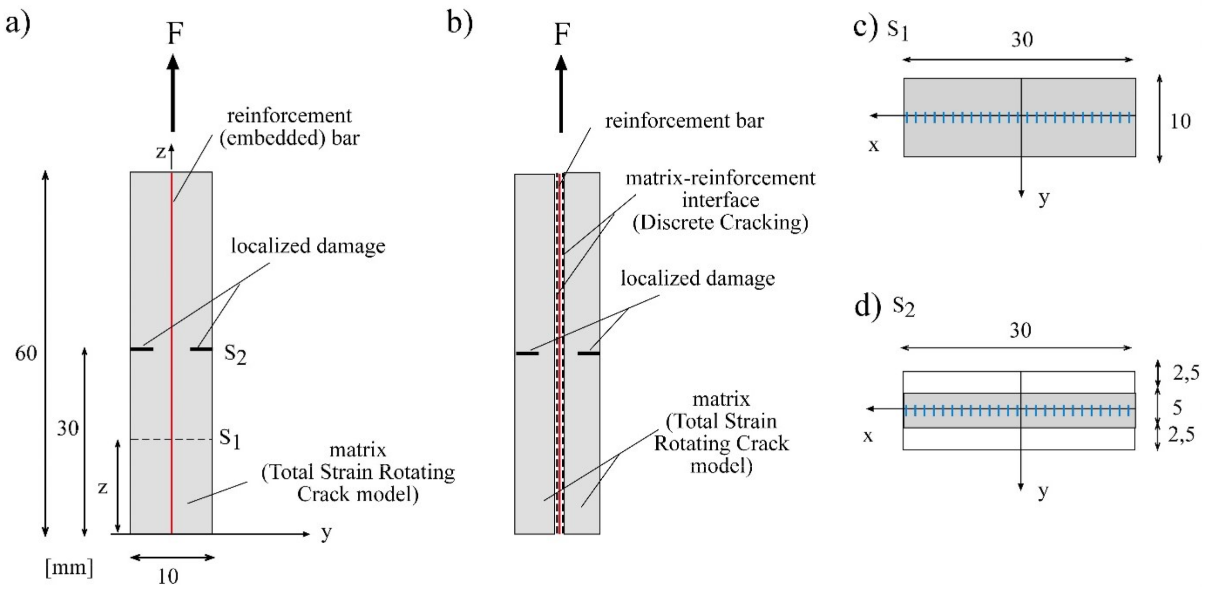


**Fig. 3. a) Macro-modelling approach; b) micro-modelling approach; c) transversal section $S_1$ of the undamaged solid; d) damaged transversal section of the solid $S_2$. Units: mm.**

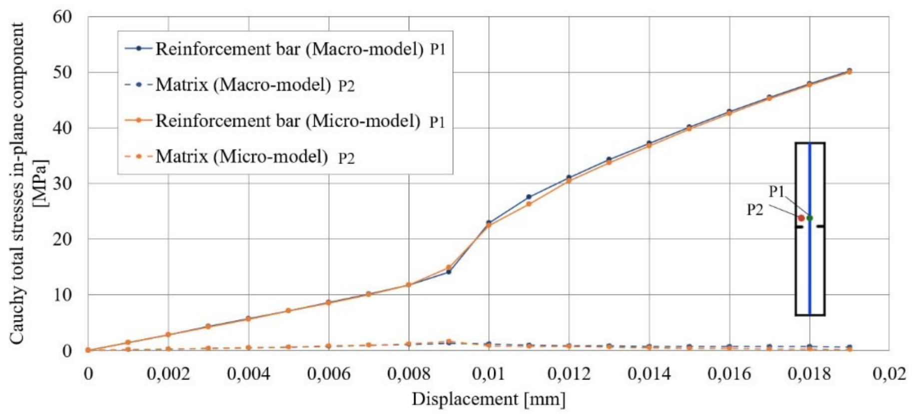


**Fig. 4_Cauchy total stresses vs displacement of the reinforcement bar and the matrix for both models.**

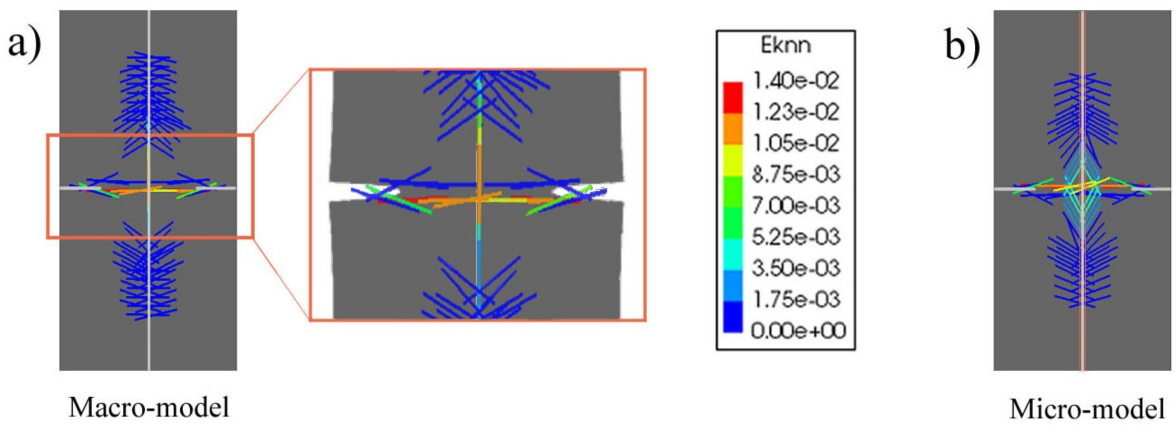


**Fig. 5. Cracks distribution for the macro- model (a) and the micro-model (b).**

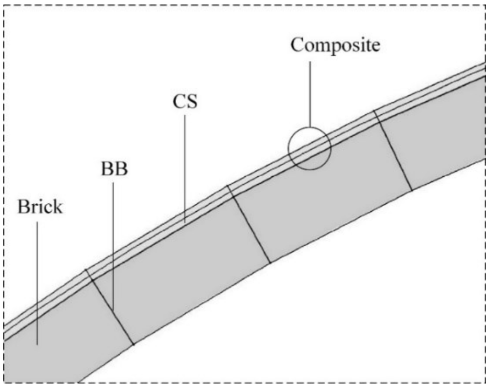


**Fig. 6. Modelling of the reinforced vault.**

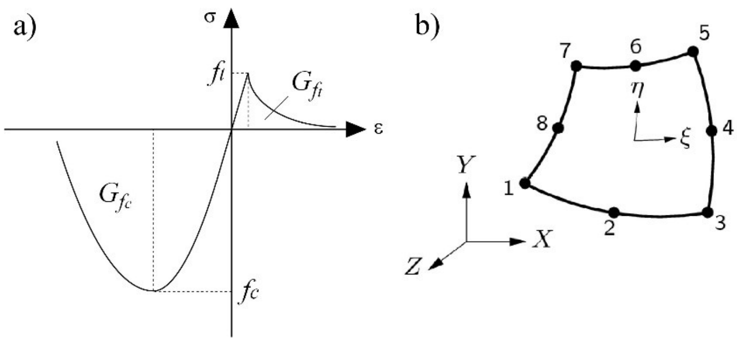


**Fig. 7. Total Strain Rotating Crack model constitutive law: exponential softening in traction and parabolic response in compression (a) and CQ16M element (c).**

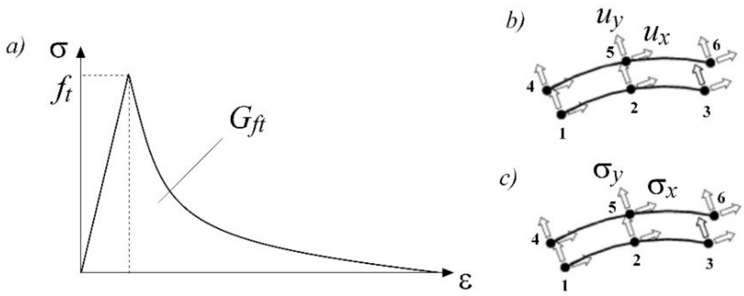


**Fig. 8. Tensile behaviour for interface elements according to** [44] **(a). 3+3 nodes interface element: displacements (b) and stresses (c).**

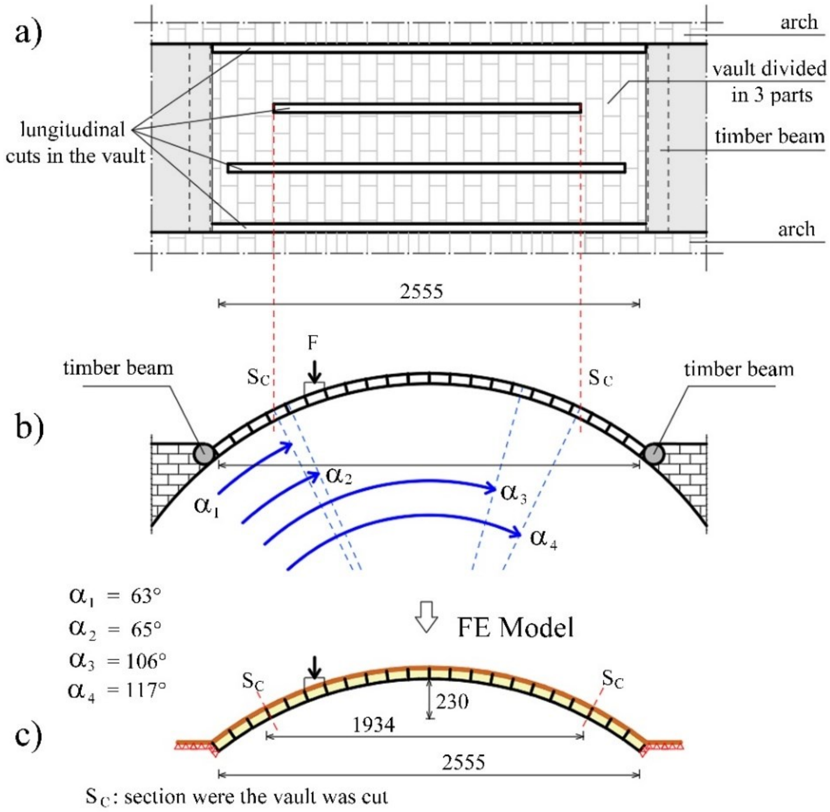


**Fig. 9. a) Tested vault. b) Hinges position for the in-situ tested FRCM reinforced vault. c) Numerical model of the tested FRCM reinforced vault.**

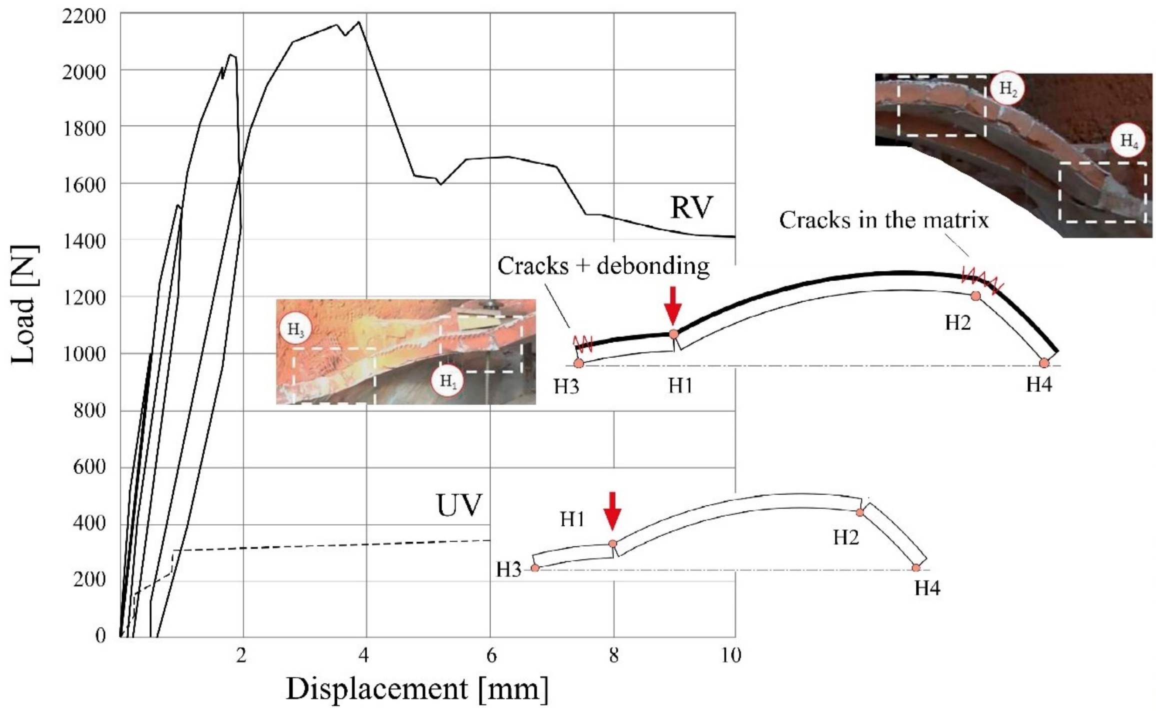


**Fig. 10. Load-displacement curves of the unstrengthened (UV) and strengthened (RV) vault. Schemes of the collapse mechanisms** [23]**.**

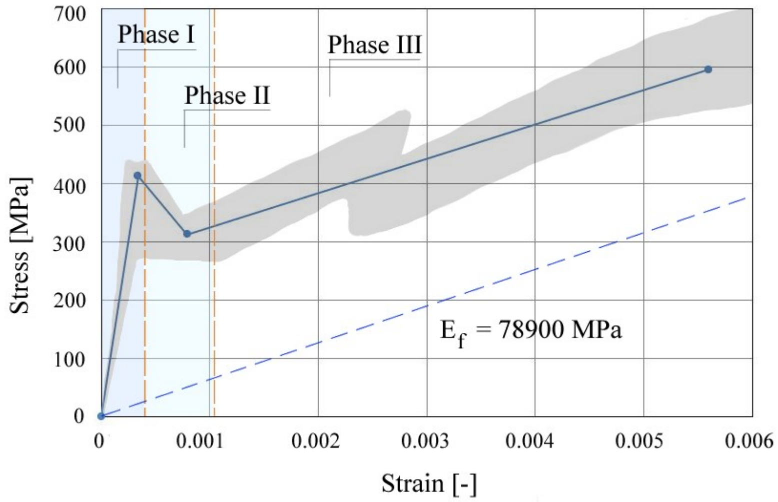


**Fig. 11. Tensile test on FRCM composite** [23].

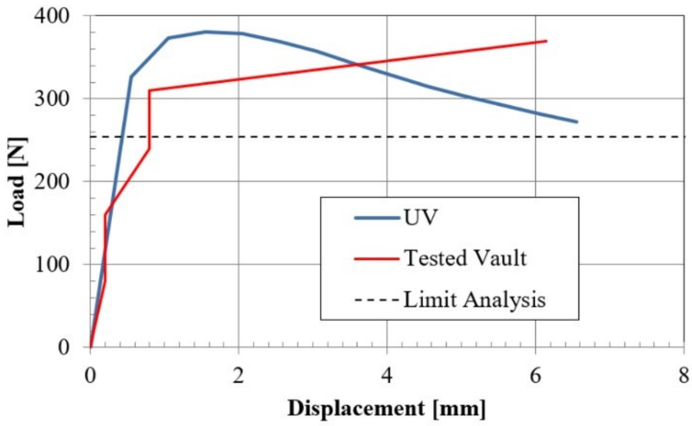


**Fig. 12. Experimental and numerical load-displacement curves for the unreinforced vault, compared to the limit load evaluated by kinematic theorem of Limit Analysis.**

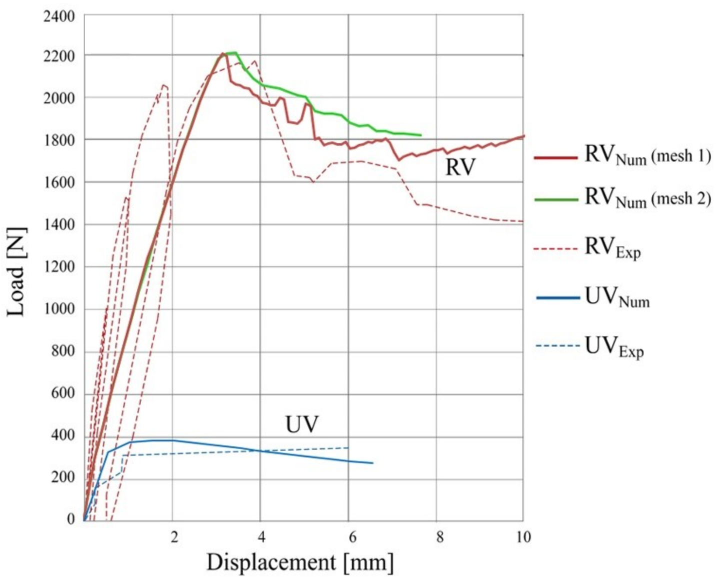

**Fig. 13. Load-displacement curves for the unreinforced (UV) and reinforced vault (RV).**

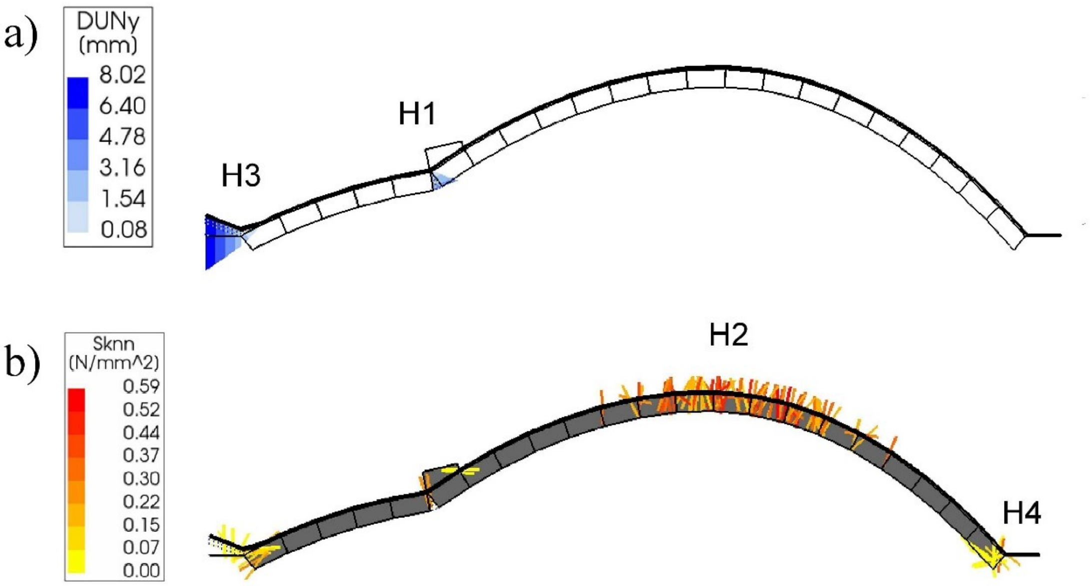


**Fig. 14. Reinforced vault (RV): relative displacements in the direction normal to the interface cracks at the collapse (a); local stresses in the direction normal to the crack (b).**

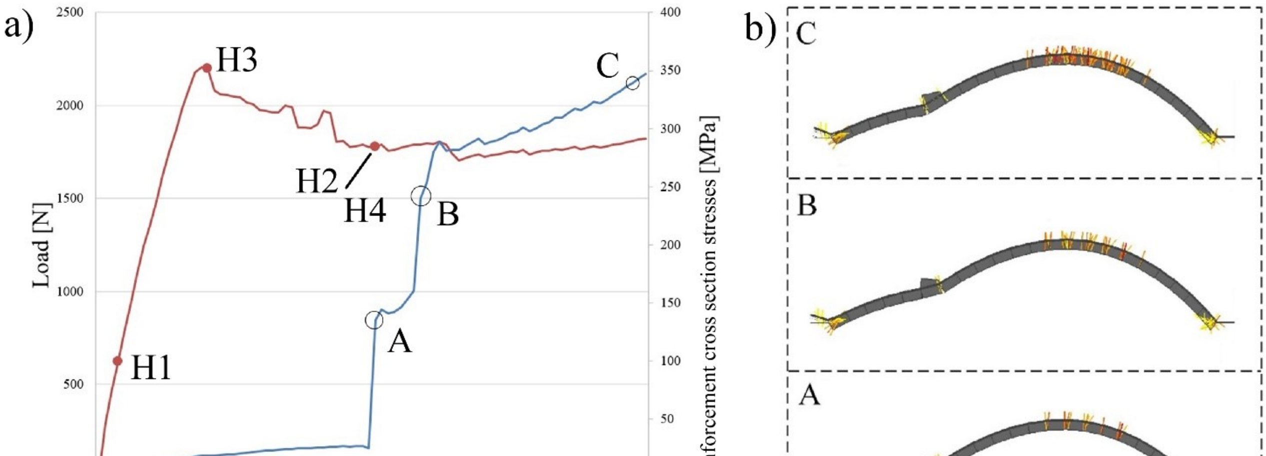


**Fig. 15. a) Load (red curve) and stress in the fibers (blue curve) vs number of the (smeared) cracks in the bricks and in the reinforcement matrix. b) Distribution of the (smeared) cracks in the bricks and in the reinforcement matrix in the three different conditions, A, B and C, marked on the blue curve in the diagram on the left.**

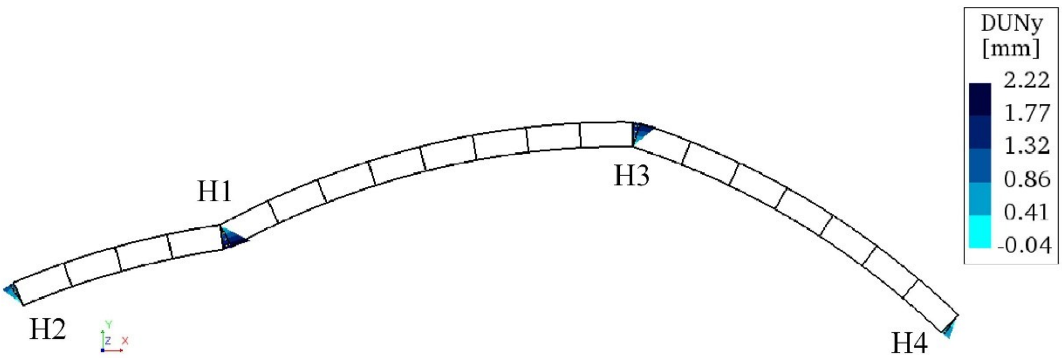


**Fig. 16. Unreinforced vault (UV): relative displacements in the direction normal to the interface cracks at the collapse.**

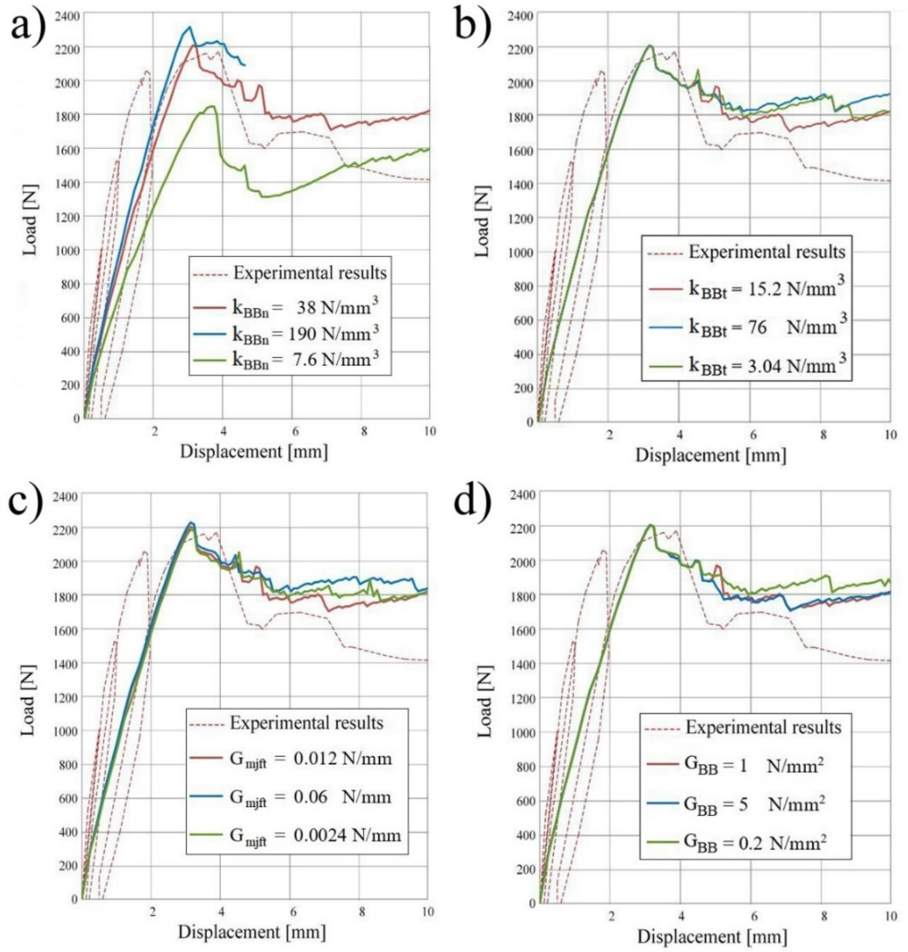


**Fig. 17. Influence of variations of BB interface normal stiffness $k_{BBn}$ (a), tangential stiffness $k_{BBt}$ (b), tensile fracture energy $G_{mjft}$ (c), shear modulus $G_{BB}$ (d).**

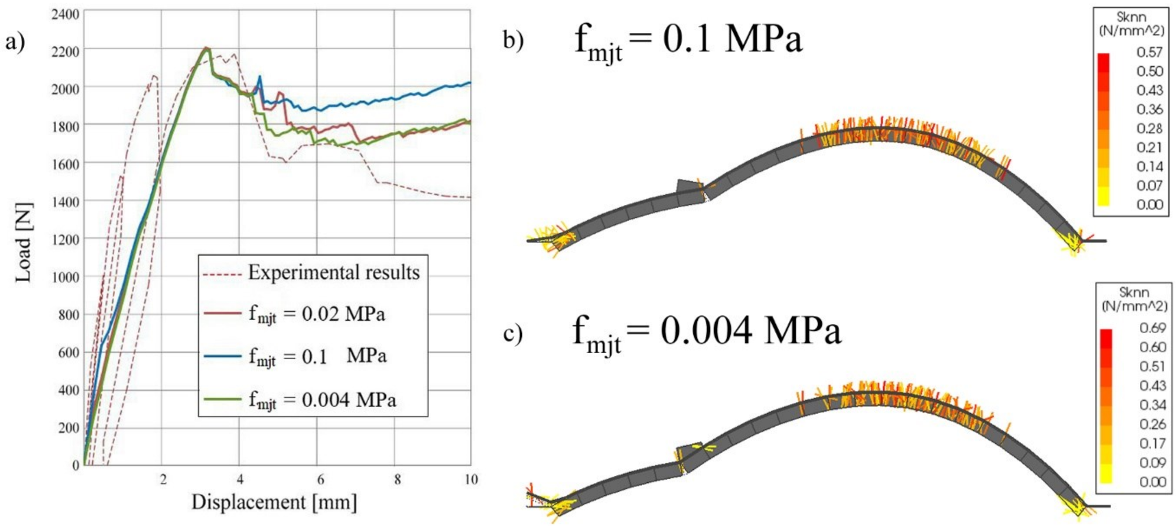


**Fig. 18. Influence of variations of BB interface tensile strength $f_{mjt}$ (a). Distribution of the local stresses in the direction normal to the crack Sknn at the collapse for $f_{mjt}$=0.1 MPa (b) and $f_{mjt}$=0.004 MPa (c).**

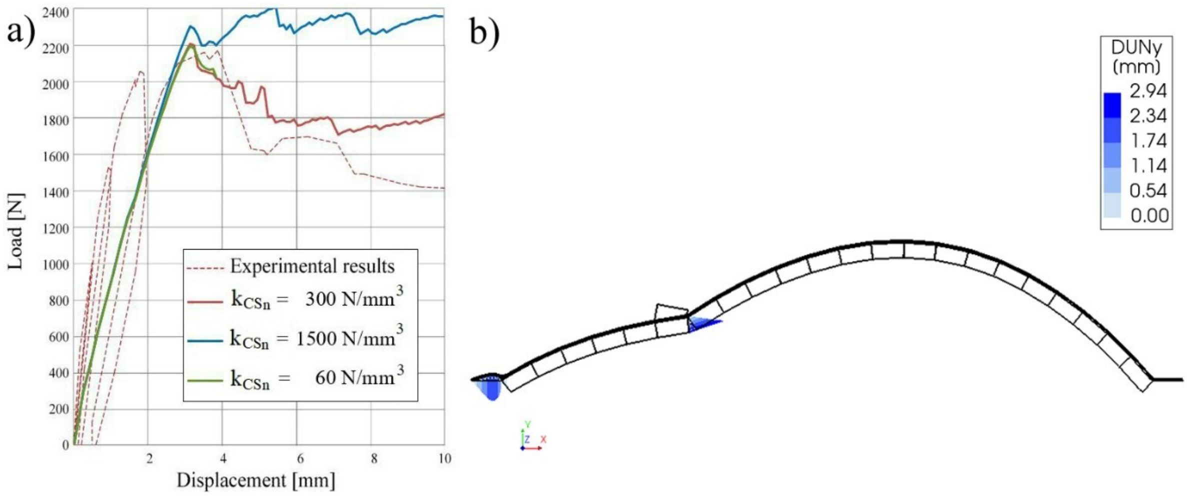


**Fig. 19. a) Influence of variations of CS interface normal stiffness $k_{CSn}$ b) Relative displacements in the direction normal to the interface cracks DUNy at the collapse.**

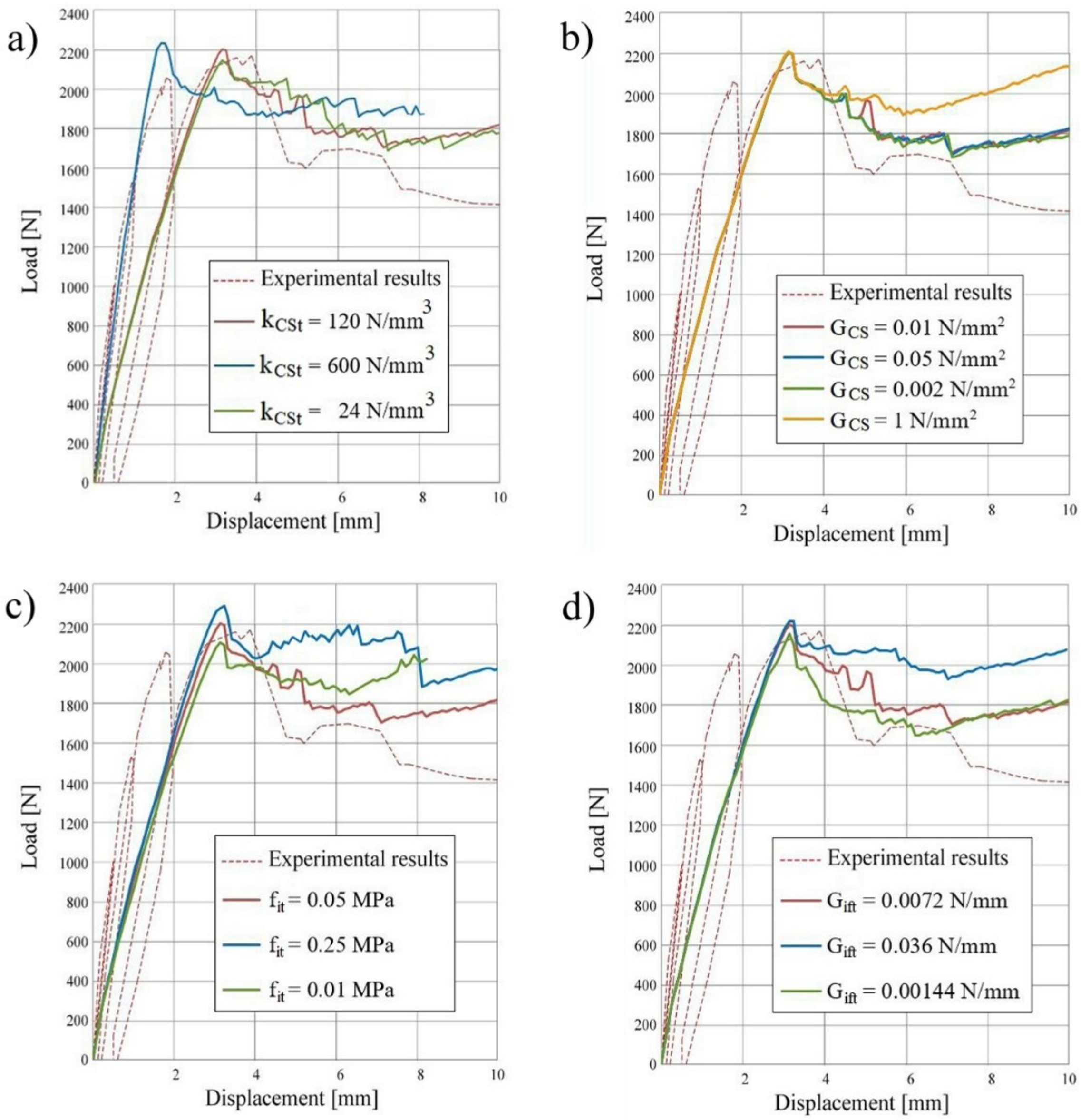


**Fig. 20. Influence of variations of CS interface tangent stiffness $k_{CSt}$ (a), reduced shear modulus $G_{CS}$ (b), tensile strength $f_{it}$ (c) and tensile fracture energy $G_{ift}$ (d).**

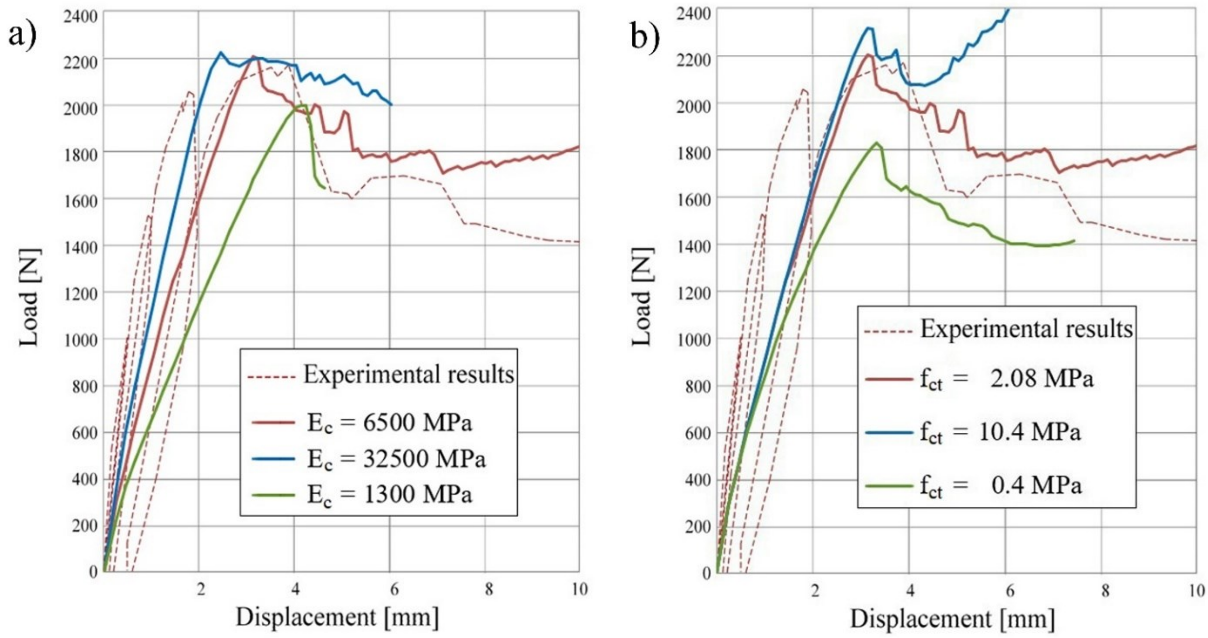


**Fig. 21. Influence of variations of FRCM matrix Young's modulus $E_c$ (a) and FRCM matrix tensile strength $f_{ct}$ (b).**

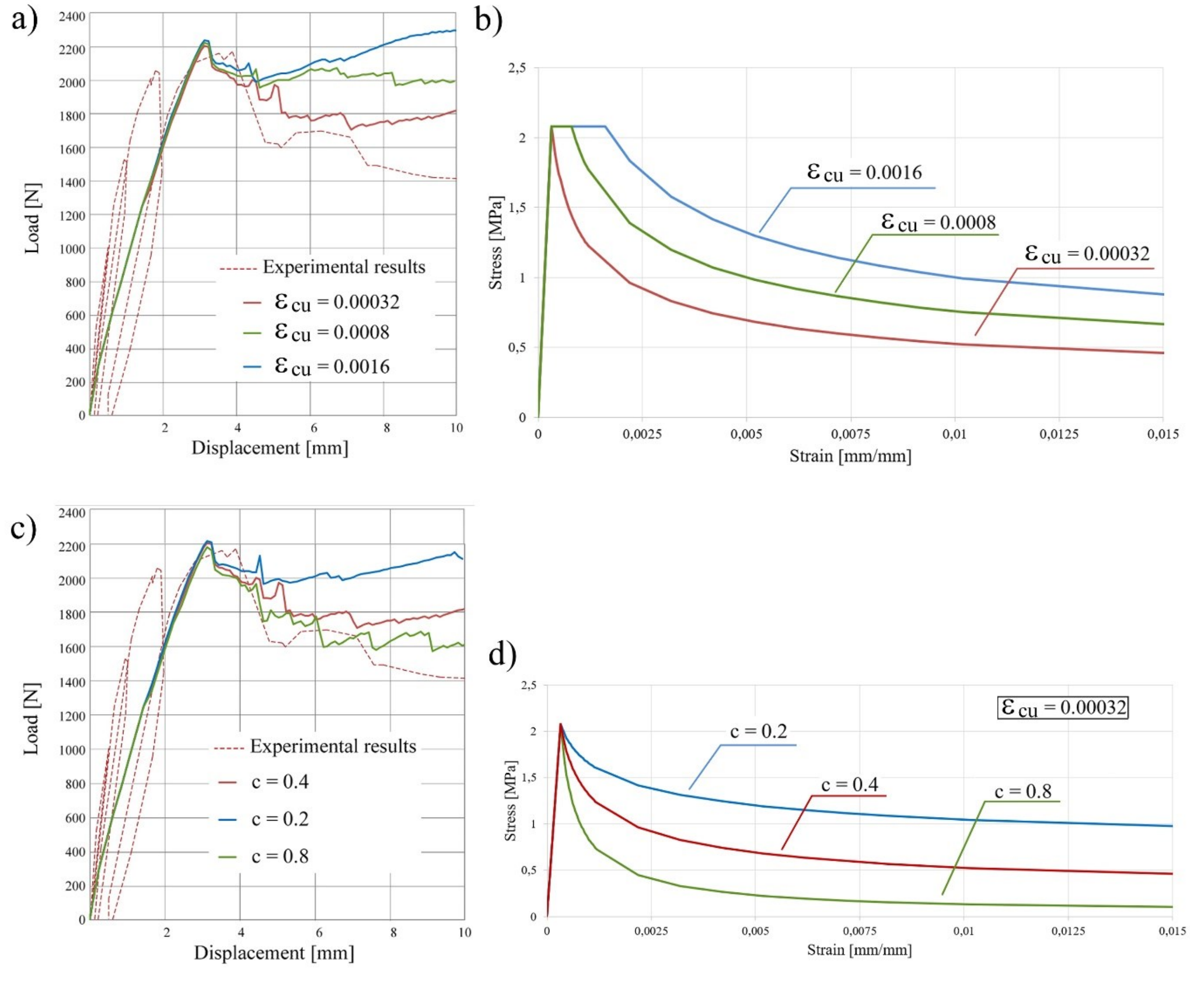


**Fig. 22. Influence of variations of plateau end strain $\varepsilon_{cu}$. (a) and of the exponent c (c); JSCE model for different values of $\varepsilon_{cu}$ (b); JSCE model for different values of the power parameter c for a fixed value of $\varepsilon_{cu}$=0.00032.**

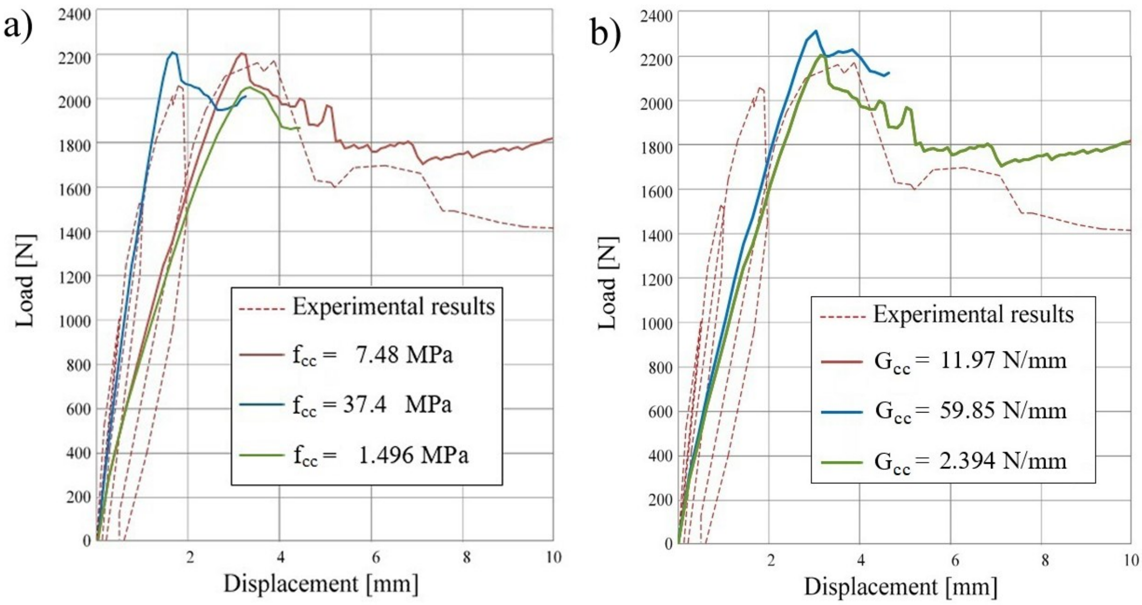


**Fig. 23. Influence of variations of the matrix compressive strength $f_{cc}$ and compressive fracture energy $G_{cc}$.**

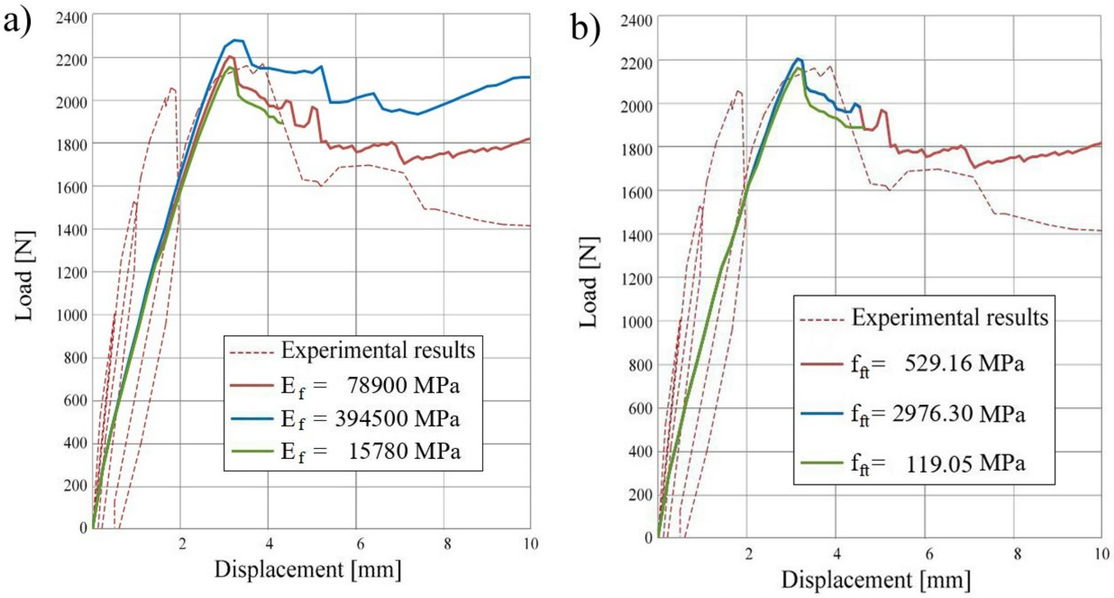


**Fig. 24. Influence of variations of the fiber mesh Young's modulus $E_f$ and the tensile strength $f_{ft}$.**

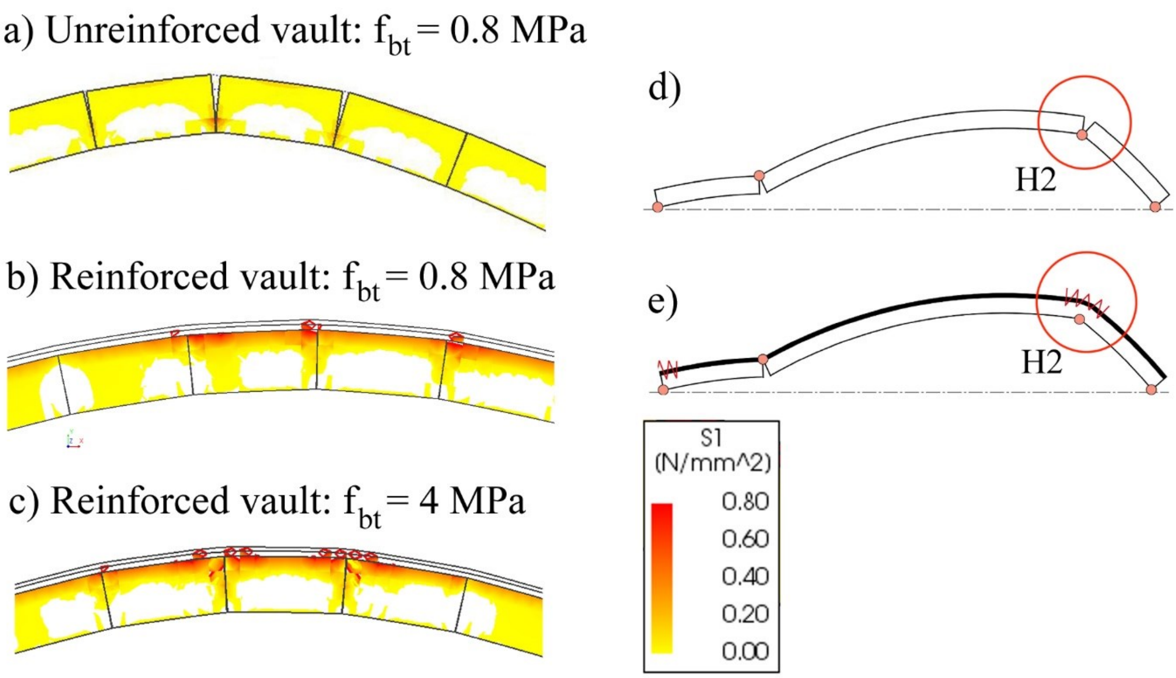


**Fig. 25. Maximum principal stresses in the bricks of the unreinforced vault (a) and reinforced vault (b/c) corresponding to hinge $H_2$ position (d/e).**

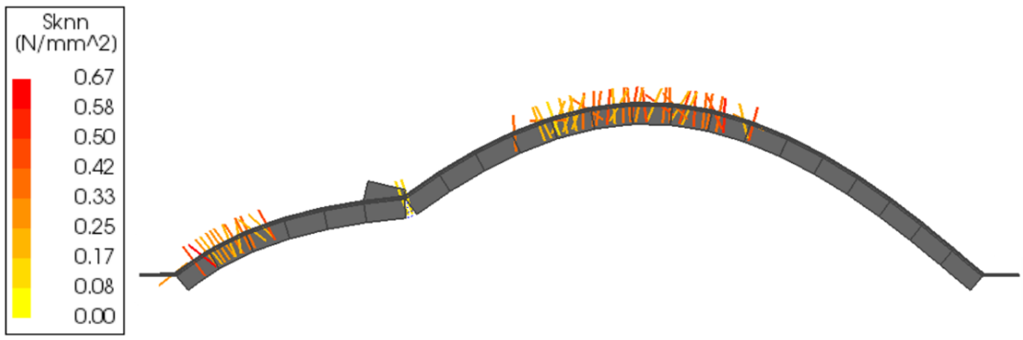


**Fig. 26. Local stresses in the direction normal to the crack at the collapse for $f_{bt}$=4 MPa.**

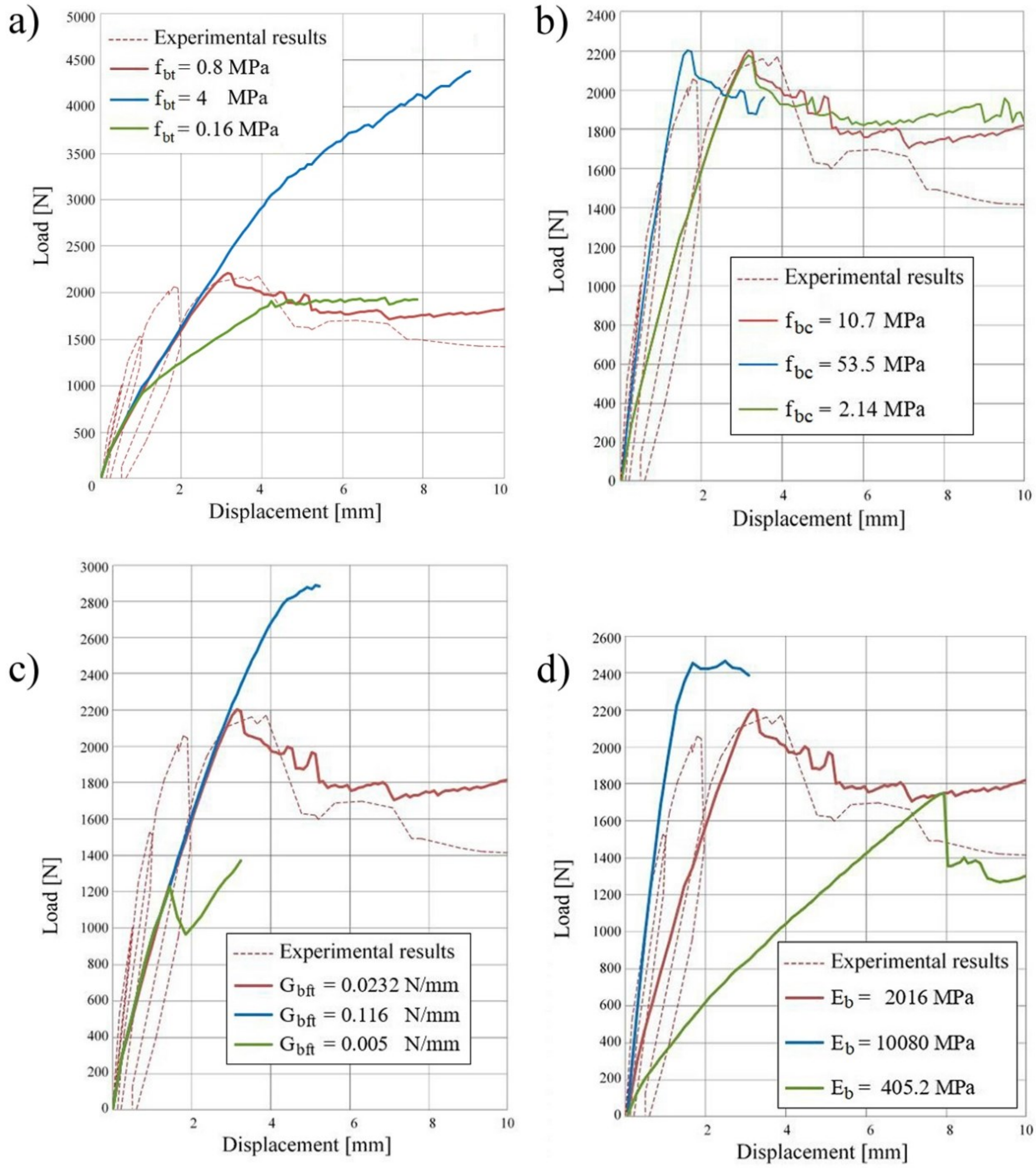


**Fig. 27. Influence of variations of bricks tensile strength $f_{bt}$ (a), compressive strength $f_{bc}$ (b), tensile fracture energy $G_{bft}$ (c), and Young's modulus $E_b$ (d).**

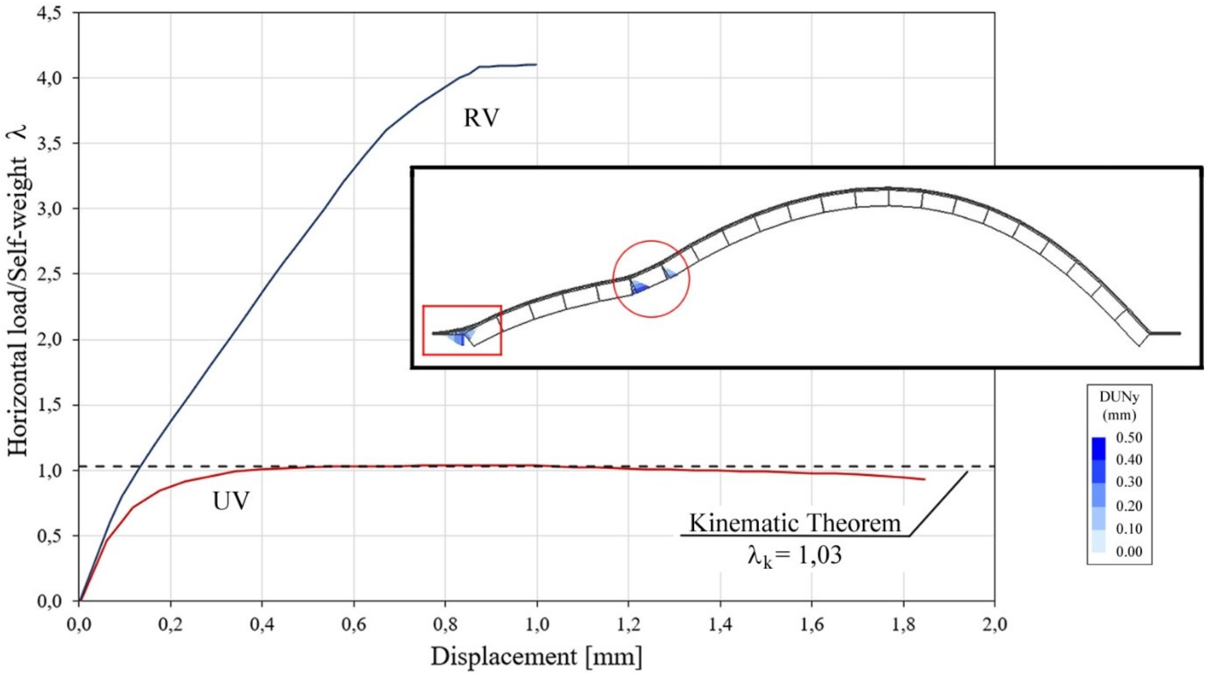


**Fig. 28. Capacity curves for the strengthened and unstrengthened vault under horizontal loads; interface relative displacement DUNy at collapse.**

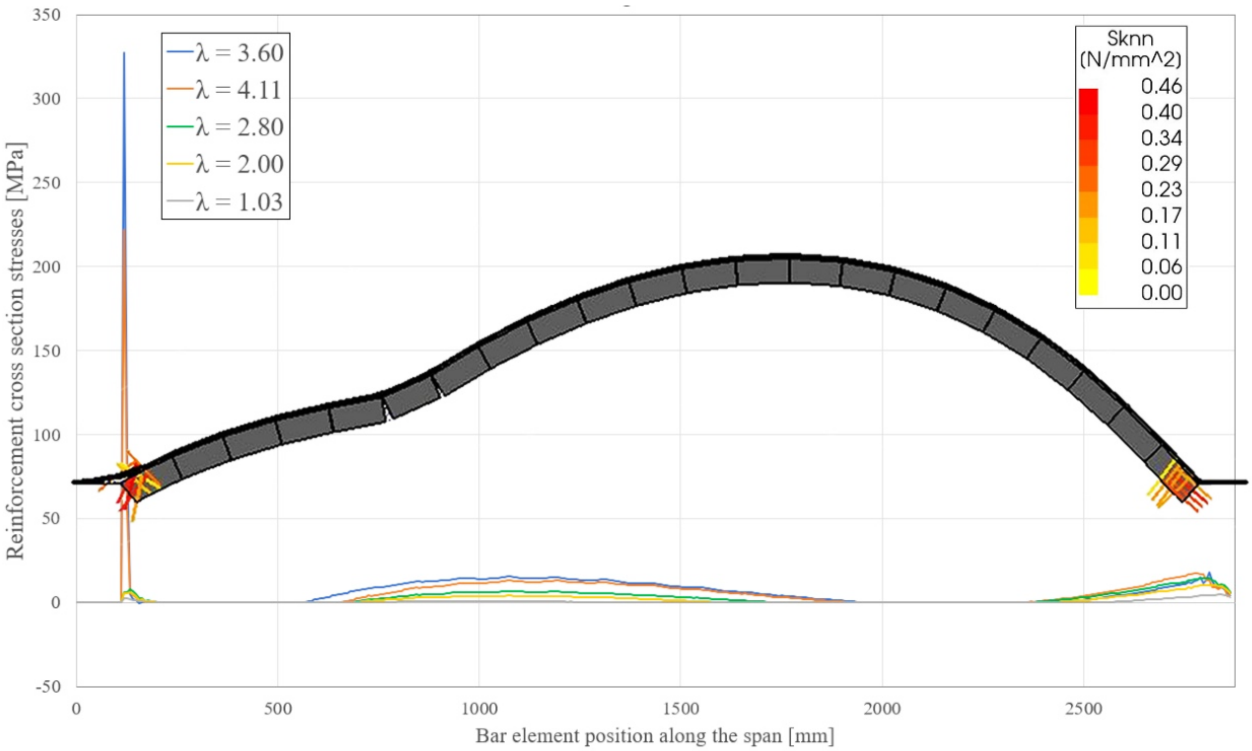


**Fig. 29_Reinforcement cross section stresses vs position of the reinforcement bar mesh element; cracks normal stresses Sknn at collapse.**